

THE 2HWC HAWC OBSERVATORY GAMMA RAY CATALOG

A.U. ABEYSEKARA,¹ A. ALBERT,² R. ALFARO,³ C. ALVAREZ,⁴ J.D. ÁLVAREZ,⁵ R. ARCEO,⁴ J.C. ARTEAGA-VELÁZQUEZ,⁵
H.A. AYALA SOLARES,⁶ A.S. BARBER,¹ N. BAUTISTA-ELIVAR,⁷ J. BECERRA GONZALEZ,⁸ A. BECERRIL,³
E. BELMONT-MORENO,³ S.Y. BENZVI,⁹ D. BERLEY,¹⁰ A. BERNAL,¹¹ J. BRAUN,¹² C. BRISBOIS,⁶ K.S. CABALLERO-MORA,⁴
T. CAPISTRÁN,¹³ A. CARRAMIÑANA,¹³ S. CASANOVA,^{14,15} M. CASTILLO,⁵ U. COTTI,⁵ J. COTZOMI,¹⁶
S. COUTIÑO DE LEÓN,¹³ E. DE LA FUENTE,¹⁷ C. DE LEÓN,¹⁶ R. DIAZ HERNANDEZ,¹³ B.L. DINGUS,² M.A. DUVERNOIS,¹²
J.C. DÍAZ-VÉLEZ,¹⁷ R.W. ELLSWORTH,¹⁸ K. ENGEL,¹⁰ D.W. FIORINO,¹⁰ N. FRAIJA,¹¹ J.A. GARCÍA-GONZÁLEZ,³
F. GARFIAS,¹¹ M. GERHARDT,⁶ A. GONZÁLEZ MUÑOZ,³ M.M. GONZÁLEZ,¹¹ J.A. GOODMAN,¹⁰ Z. HAMPEL-ARIAS,¹²
J.P. HARDING,² S. HERNANDEZ,³ A. HERNANDEZ-ALMADA,³ J. HINTON,¹⁵ C.M. HUI,¹⁹ P. HÜNTEMEYER,⁶ A. IRIARTE,¹¹
A. JARDIN-BLICQ,¹⁵ V. JOSHI,¹⁵ S. KAUFMANN,⁴ D. KIEDA,¹ A. LARA,²⁰ R.J. LAUER,²¹ W.H. LEE,¹¹ D. LENNARZ,²²
H. LEÓN VARGAS,³ J.T. LINNEMANN,²³ A.L. LONGINOTTI,¹³ G. LUIS RAYA,⁷ R. LUNA-GARCÍA,²⁴ R. LÓPEZ-COTO,¹⁵
K. MALONE,²⁵ S.S. MARINELLI,²³ O. MARTINEZ,¹⁶ I. MARTINEZ-CASTELLANOS,¹⁰ J. MARTÍNEZ-CASTRO,²⁴
H. MARTÍNEZ-HUERTA,²⁶ J.A. MATTHEWS,²¹ P. MIRANDA-ROMAGNOLI,²⁷ E. MORENO,¹⁶ M. MOSTAFÁ,²⁵ L. NELLEN,²⁸
M. NEWBOLD,¹ M.U. NISA,⁹ R. NORIEGA-PAPAQUI,²⁷ R. PELAYO,²⁴ J. PRETZ,²⁵ E.G. PÉREZ-PÉREZ,⁷ Z. REN,²¹
C.D. RHO,⁹ C. RIVIÈRE,¹⁰ D. ROSA-GONZÁLEZ,¹³ M. ROSENBERG,²⁵ E. RUIZ-VELASCO,³ H. SALAZAR,¹⁶
F. SALESA GREUS,¹⁴ A. SANDOVAL,³ M. SCHNEIDER,²⁹ H. SCHOORLEMMER,¹⁵ G. SINNIS,² A.J. SMITH,¹⁰ R.W. SPRINGER,¹
P. SURAJBALI,¹⁵ I. TABOADA,²² O. TIBOLLA,⁴ K. TOLLEFSON,²³ I. TORRES,¹³ T.N. UKWATTA,² G. VIANELLO,³⁰
L. VILLASEÑOR,⁵ T. WEISGARBER,¹² S. WESTERHOFF,¹² I.G. WISHER,¹² J. WOOD,¹² T. YAPICI,²³ P.W. YOUNK,²
A. ZEPEDA,^{26,4} AND H. ZHOU²

¹Department of Physics and Astronomy, University of Utah, Salt Lake City, UT, USA

²Physics Division, Los Alamos National Laboratory, Los Alamos, NM, USA

³Instituto de Física, Universidad Nacional Autónoma de México, Mexico City, Mexico

⁴Universidad Autónoma de Chiapas, Tuxtla Gutiérrez, Chiapas, Mexico

⁵Universidad Michoacana de San Nicolás de Hidalgo, Morelia, Mexico

⁶Department of Physics, Michigan Technological University, Houghton, MI, USA

⁷Universidad Politécnica de Pachuca, Pachuca, Hidalgo, Mexico

⁸NASA Goddard Space Flight Center, Greenbelt, MD, USA

⁹Department of Physics & Astronomy, University of Rochester, Rochester, NY, USA

¹⁰Department of Physics, University of Maryland, College Park, MD, USA

¹¹Instituto de Astronomía, Universidad Nacional Autónoma de México, Mexico City, Mexico

¹²Department of Physics, University of Wisconsin-Madison, Madison, WI, USA

¹³Instituto Nacional de Astrofísica, Óptica y Electrónica, Tonantzintla, Puebla, Mexico

¹⁴Instytut Fizyki Jadrowej im Henryka Niewodniczańskiego Polskiej Akademii Nauk, Krakow, Poland

¹⁵Max-Planck Institute for Nuclear Physics, Heidelberg, Germany

¹⁶Facultad de Ciencias Físico Matemáticas, Benemérita Universidad Autónoma de Puebla, Puebla, Mexico

¹⁷Departamento de Física, Centro Universitario de Ciencias Exactas e Ingenierías, Universidad de Guadalajara, Guadalajara, Mexico

¹⁸School of Physics, Astronomy, and Computational Sciences, George Mason University, Fairfax, VA, USA

¹⁹NASA Marshall Space Flight Center, Astrophysics Office, Huntsville, AL, USA

²⁰Instituto de Geofísica, Universidad Nacional Autónoma de México, Mexico City, Mexico

²¹Department of Physics and Astronomy, University of New Mexico, Albuquerque, NM, USA

²²School of Physics and Center for Relativistic Astrophysics, Georgia Institute of Technology, Atlanta, GA, USA

²³Department of Physics and Astronomy, Michigan State University, East Lansing, MI, USA

²⁴Centro de Investigación en Computación, Instituto Politécnico Nacional, Mexico City, Mexico

²⁵Department of Physics, Pennsylvania State University, University Park, PA, USA

²⁶Physics Department, Centro de Investigación y de Estudios Avanzados del IPN, Mexico City, Mexico

²⁷ *Universidad Autónoma del Estado de Hidalgo, Pachuca, Mexico*

²⁸ *Instituto de Ciencias Nucleares, Universidad Nacional Autónoma de México, Mexico City, Mexico*

²⁹ *Santa Cruz Institute for Particle Physics, University of California, Santa Cruz, Santa Cruz, CA, USA*

³⁰ *Department of Physics, Stanford University, Stanford, CA, USA*

ABSTRACT

We present the first catalog of TeV gamma-ray sources realized with the recently completed High Altitude Water Cherenkov Observatory (HAWC). It is the most sensitive wide field-of-view TeV telescope currently in operation, with a 1-year survey sensitivity of $\sim 5\text{--}10\%$ of the flux of the Crab Nebula. With an instantaneous field of view >1.5 sr and $>90\%$ duty cycle, it continuously surveys and monitors the sky for gamma ray energies between hundreds GeV and tens of TeV.

HAWC is located in Mexico at a latitude of 19° North and was completed in March 2015. Here, we present the 2HWC catalog, which is the result of the first source search realized with the complete HAWC detector. Realized with 507 days of data and represents the most sensitive TeV survey to date for such a large fraction of the sky. A total of 39 sources were detected, with an expected contamination of 0.5 due to background fluctuation. Out of these sources, 16 are more than one degree away from any previously reported TeV source. The source list, including the position measurement, spectrum measurement, and uncertainties, is reported. Seven of the detected sources may be associated with pulsar wind nebulae, two with supernova remnants, two with blazars, and the remaining 23 have no firm identification yet.

1. INTRODUCTION

The High Altitude Water Cherenkov Observatory (HAWC) is a newly completed very high energy (VHE; >100 GeV) gamma-ray observatory with a 1-year survey sensitivity of ~ 5 – 10% of the flux of the Crab Nebula. The variation in sensitivity depends on the declination of the source under consideration over the observable sky, with declinations between -20° and 60° for the present study. Unlike imaging atmospheric Cherenkov telescopes (IACTs), such as H.E.S.S. (Aharonian et al. 2004), MAGIC (Aleksić et al. 2016), VERITAS (Holder et al. 2006), and FACT (Anderhub et al. 2011) which observe the Cherenkov light emitted by the extensive air showers as they develop in the atmosphere, HAWC detects particles of these air showers that reach ground level, allowing it to operate continuously and observe an instantaneous field of view of >1.5 sr. Prior to this work, unbiased VHE surveys were conducted by the Milagro (Atkins et al. 2003; Atkins et al. 2004) and ARGO (Bacci et al. 2002) collaborations. Compared to these previous surface arrays, the sensitivity of HAWC is improved by more than an order of magnitude thanks to a combination of large size, high elevation, and unique background rejection capability. These features make HAWC ideally suited as a VHE survey instrument. High-sensitivity surveys of portions of the Galactic Plane have also been published by H.E.S.S. (Aharonian et al. 2006b), MAGIC (Albert et al. 2006) and VERITAS (Popkow et al. 2015). At lower energies, the Large Area Telescope on the space-based Fermi Observatory (*Fermi*-LAT) has detected many thousands of Galactic and extragalactic gamma-ray sources (Acero et al. 2015), but its small size limits its reach into the VHE band. The work presented here is the most sensitive comprehensive sky survey carried out above 1 TeV.

There are about 200 known VHE gamma-ray sources detected at high significance by a number of observatories (e.g. TeVCat catalog; Wakely & Horan 2008).

Within the Galaxy, the VHE sources include pulsar wind nebula (PWNe), supernova remnants (SNRs), binary systems, and diffuse emission from the Galactic plane. The SNRs and PWNe represent the majority of the identified sources. Most Galactic gamma-ray sources have power-law spectra consistent with shock acceleration of electrons, though there is considerable evidence for gamma-ray production by hadronic cosmic rays interacting with matter. Most Galactic sources are observed as spatially extended by IACTs (Carrigan et al. 2013).

Beyond our galaxy, almost all known TeV sources are Active Galactic Nuclei (AGNs) and most of them are categorized as blazars. The TeV gamma-ray emission is

generally observed to be variable and thought to originate from one or multiple regions of particle acceleration in the jet. While gamma-ray emission has been observed up to energies of about 10 TeV for some blazars (Acciari et al. 2011; Aharonian et al. 2001), the flux at and beyond such energies is strongly attenuated as a function of distance due to photon-photon interaction with the extragalactic background light (EBL). Since the sensitivity of HAWC peaks around 10 TeV (depending on the source spectrum and declination, see Section 4.1 for details), where absorption of TeV photons through the infrared component of the EBL becomes severe, the sensitivity of the HAWC survey to distant AGNs is relatively poor.

Many VHE sources are not unambiguously associated with objects identified at other wavelengths (a fifth of TeVCat sources are reported as unidentified). Further spectral and morphological studies are required to understand their origins and emission mechanisms.

In addition to a peak sensitivity at higher energies, the angular resolution of HAWC is larger than the IACT's. Consequently, comparison of source significance and flux with IACT observations requires careful examination. For example, the HAWC instrument is relatively more sensitive to sources with harder energy spectra than softer ones, and to extended sources than pointlike sources. On the other hand, the surface detection method employed by HAWC permits continuous observation of the entire overhead sky, both during the day and night and under all weather conditions. For sources that transit through its field of view, HAWC typically accumulates 1500–2000 hours/yr of total exposure. Thus, above 10 TeV where photon statistics are poor, HAWC achieves better sensitivity than even long-duration observations by IACTs.

This paper presents a catalog of TeV gamma-ray sources resulting from a search for significantly enhanced point and extended emission detected in the gamma-ray sky maps of 17 months of HAWC data. More detailed morphology studies will be the subject of future papers.

In Section 2, we describe the HAWC detector. Section 3 describes the analysis of gamma-ray events and the construction of our source catalog. Results and discussion are provided in Sections 4, 5, and 6, and conclusions and outlook in Section 7.

2. HAWC DETECTOR

The HAWC detector is located in central Mexico at $18^\circ 59' 41''$ N $97^\circ 18' 30.6''$ W and an elevation of 4100 m a.s.l. The instrument comprises 300 identical water Cherenkov detectors (WCDs) made from 5 m high, 7.32 m diameter commercial water storage tanks. Each

tank contains a custom-made light-tight bladder to accommodate 190,000 liters of purified water. Four upward facing photomultiplier tubes (PMTs) are mounted at the bottom of each tank: a 10" Hamamatsu R7081-HQE PMT positioned at the center and three 8" Hamamatsu R5912 PMTs which are positioned halfway between the tank center and rim. The central PMT has roughly twice the sensitivity of the outer PMTs due to its superior quantum efficiency and its larger size. The WCDs are filled to a depth of 4.5 m, with 4.0 m (more than 10 radiation lengths) of water above the PMTs. This large depth guarantees that the electrons, positrons, and gammas in the air shower are fully absorbed by the HAWC detector well above the PMT level, so that the detector itself acts as an electromagnetic (EM) calorimeter providing an accurate measurement of EM energy deposition. High-energy electrons are detected via the Cherenkov light they produce in the water and gamma rays are converted to electrons through pair production and Compton scattering. Muons are also detected. They are more likely to be produced in air showers originating from hadronic cosmic-ray interactions with the atmosphere and tend to have higher transverse momentum producing large signals in the PMTs far from the air shower axis and thus serve as useful tags for rejecting hadronic backgrounds. The WCDs are arranged in a compact layout to maximize the density of the sensitive area, with about 60% of the 22,000 m² detector area instrumented. See Figure 1 for a diagram of the HAWC detector.

Analog signals from the PMTs are transmitted by RG-59 coaxial cable to a central counting house. The signals are shaped and discriminated at two voltage thresholds roughly corresponding to 1/4 PE and 4 PEs and the threshold crossing times (both rising and falling) are recorded using CAEN V1190A time-to-digital converters. Individual signals that pass at least the low threshold are called hits. The time-over-threshold is used to estimate the charge. The response of this system is roughly logarithmic, so that the readout has reasonable charge resolution over a very wide dynamic range, from a fraction of 1 PE to 10,000 PEs. The timing resolution for large pulses is better than 1 ns. All channels are read out in real time with zero dead time and blocks of data are aggregated in a real-time computing farm. A trigger is generated when a sufficient number of PMTs record a hit within a 150 ns window (28 hits were required for most of the data used in this analysis, though other values were occasionally used earlier). This results in a ~ 20 kHz trigger rate. Small events, with a number of hits close to the threshold value and which dominate the triggers, require a specific treatment and are removed from the

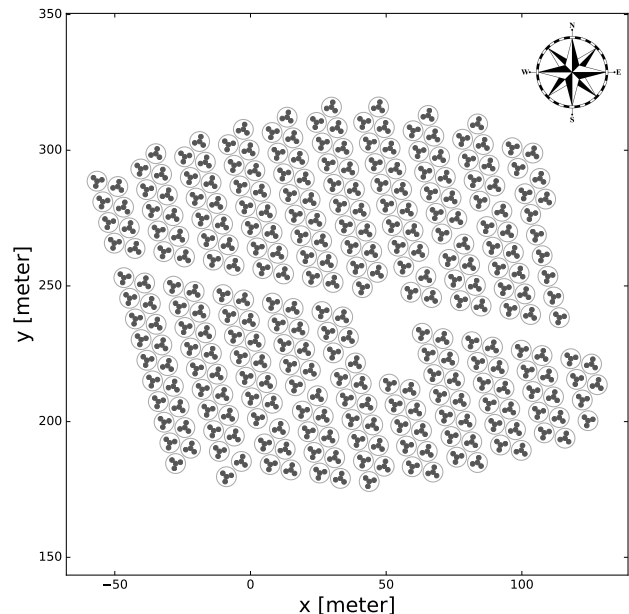


Figure 1. Layout of HAWC WCDs and positions of the PMTs (PMTs not to scale). The conspicuous gap indicates the location of the counting house, which is centrally located to minimize the cable length.

analysis presented here. In the future their inclusion will significantly lower the energy threshold of HAWC. For sources with spectra that extend beyond 1 TeV, like the Crab Nebula, the sensitivity usually peaks above 5 TeV (depending on the source spectrum and declination) and excluding the near-threshold events does not significantly reduce the sensitivity. Details of the event selection for the present analysis are presented in the next section.

For each triggered event, the parameters of the air shower, like the direction, the size, and some gamma/hadron separation variables, are extracted from the recorded hit times and amplitudes, using a shower model developed through the study of Monte Carlo simulations and optimized using observations of the Crab Nebula (Abeysekara et al. 2017, submitted to ApJ). The angular resolution of the HAWC instrument varies with the event size (number of hit PMTs) and ranges from $\sim 0.2^\circ$ (68% containment) for large events events hitting almost all the PMTs to $\sim 1.0^\circ$ for events near the analysis threshold.

Gamma-ray induced showers are generally compact and have a smooth lateral distribution around the shower core (the position where the shower axis intersects the detector plane). In contrast, hadronic background events tend to be broader, contain multiple or poorly defined cores, and include highly localized large signals from muons and hadrons at significant distance

from the shower axis. Selection cuts on shower morphology eliminate >99% of the hadronic background in the large event size samples and at least 85% of the background near the analysis threshold, while usually retaining more than 50% of the gamma-ray induced signal events. Details of the data reconstruction, and analysis, and the verification of the sensitivity of the measurement will be presented in a future publication on the observation of the Crab Nebula with the HAWC Observatory (Abeysekara et al. 2017, submitted to ApJ).

3. METHODOLOGY

In this section we review the details of the dataset used in the analysis and describe the event selection and the construction of unbiased maps of the viewable sky, which include estimates of the cosmic-ray background rates. From the maps we compute a test statistic (TS) from the ratio of the likelihood that a source is present and the null hypotheses that the observed event population is due to background alone. We identify and localize sources from a list of local maxima in the TS maps with values greater than 25. The procedure is applied to the map to identify pointlike sources as well as sources with characteristic sizes 0.25° , 0.5° , 1° , and 2° . Many sources, particularly the bright ones, will likely be detected in both the point-source and extended-source maps. We find that there are some extended regions of gamma-ray emission that could either be interpreted as a single extended source or an ensemble of point sources. Below we describe the method employed to detect point and extended sources, to estimate their positions, extents, and spectra and finally discuss the principal sources of systematic uncertainty.

3.1. Dataset

The results presented here are obtained using data taken between 2014-11-26 and 2016-06-02. During this period, 8.8×10^{11} triggered events were recorded to disk. The full HAWC Observatory was inaugurated in 2015 March. During the construction phase prior to the inauguration, data were collected with a variable number of WCDs ranging from 250 to 300. Overall there was downtime of 40 days (7.2%) during this 553 day period, for the most part related to power issues or scheduled shutdowns for construction or maintenance. In addition, 7 days of data (1.3%) were removed based on requirements regarding the stability of the detector performance. The final livetime used for the analysis is 506.6 days, corresponding to 92% duty cycle.

The data were reconstructed and analyzed with *Pass 4*, which includes improved calibrations, improved

event reconstruction, and improvements in the likelihood framework used for the map analysis. The new event reconstruction benefits from a directional fit using an improved shower model, a new algorithm to separate gamma-ray and hadronic events, and a better electronics model. For comparison, our previous search for sources in the inner Galactic Plane which defined the 1HWC source list (Abeysekara et al. 2016) was performed using 275 days of data taken with a detector consisting of about one third of the full HAWC array and using the *Pass 1* analysis. This new pass, combined with the larger detector and longer exposure time, improves the sensitivity of the survey by about a factor of 5 with respect to the *Pass 1* inner Galactic Plane search.

3.2. Event Selection

Events are classified by size in nine analysis bins \mathcal{B} , presented in Table 1, depending on the fraction f_{hit} of active PMTs in the detector that participate in the reconstruction of the air shower. We chose to define bins based on the fraction of the detector hit, rather than the absolute number of PMTs, in order to obtain more stable results for the various detector configurations of active WCDs over time.

The selection cuts on the gamma/hadron separation variables are optimized for each bin using observations of the Crab Nebula (Abeysekara et al. 2017, submitted to ApJ). The point spread function (PSF) of the reconstructed events depends on the event size. In Table 1, the ψ_{68} column represents the 68% containment angle of the PSF, for a source similar to the Crab Nebula. Large events have a better PSF, a better hadronic background rejection, and correspond to higher energy primary particles. The efficiency of the gamma/hadron separation cuts is indicated in the $\epsilon_\gamma^{\text{MC}}$ and $\epsilon_{\text{CR}}^{\text{data}}$ columns, where the gamma efficiency has been estimated using Monte Carlo simulation of the detector and the hadron efficiency has been measured directly using cosmic ray data. The $\tilde{E}_\gamma^{\text{MC}}$ column represents the median energy of the simulated gamma-ray photons in this analysis bin for a source at a declination of 20° and for an energy spectrum $E^{-2.63}$ (Crab-Nebula-like source). Events in the same bin for a source with a harder spectrum or at larger declination will tend to have a larger energy on average.

3.3. Event and Background Maps

After reconstruction, event and background maps are generated. The event maps are simply histograms of the arrival direction of the reconstructed events, in the equatorial coordinate system. The background maps are computed using a method developed for the Milagro experiment known as direct integration (Atkins

Table 1. Properties of the nine analysis bins: bin number \mathcal{B} , event size f_{hit} , 68% PSF containment ψ_{68} , cut selection efficiency for gammas $\epsilon_{\gamma}^{\text{MC}}$ and cosmic rays $\epsilon_{\text{CR}}^{\text{data}}$, and median energy for a reference source of spectral index -2.63 at a declination of 20° $\tilde{E}_{\gamma}^{\text{MC}}$.

| \mathcal{B} | f_{hit} (%) | ψ_{68} ($^\circ$) | $\epsilon_{\gamma}^{\text{MC}}$ (%) | $\epsilon_{\text{CR}}^{\text{data}}$ (%) | $\tilde{E}_{\gamma}^{\text{MC}}$ (TeV) |
|---------------|-------------------------|-----------------------------|--|---|---|
| 1 | 6.7 – 10.5 | 1.03 | 70 | 15 | 0.7 |
| 2 | 10.5 – 16.2 | 0.69 | 75 | 10 | 1.1 |
| 3 | 16.2 – 24.7 | 0.50 | 74 | 5.3 | 1.8 |
| 4 | 24.7 – 35.6 | 0.39 | 51 | 1.3 | 3.5 |
| 5 | 35.6 – 48.5 | 0.30 | 50 | 0.55 | 5.6 |
| 6 | 48.5 – 61.8 | 0.28 | 35 | 0.21 | 12 |
| 7 | 61.8 – 74.0 | 0.22 | 63 | 0.24 | 15 |
| 8 | 74.0 – 84.0 | 0.20 | 63 | 0.13 | 21 |
| 9 | 84.0 – 100.0 | 0.17 | 70 | 0.20 | 51 |

et al. 2003). It is used to fit the isotropic distribution of events that pass the gamma-ray event selection, while accounting for the asymmetric detector angular response and varying all-sky rate. As strong gamma-ray sources would bias the background estimate, some regions are excluded from the computation. These regions cover the Crab, the two Markarians, the Geminga region and, a region $\pm 3^\circ$ around the inner Galactic Plane. Nine event maps and nine background maps are generated, for the nine analysis bins.

The maps are produced using a HEALPix pixelization scheme (Górski et al. 2005), where the sphere is divided in 12 equal area base pixels, each of which is subdivided into a grid of $N_{\text{side}} \times N_{\text{side}}$. For the present analysis, maps were initially done using $N_{\text{side}} = 1024$ for a mean spacing between pixel centers of less than 0.06° , which is small compared to the typical PSF of the reconstructed events as shown on Table 1.

3.4. Source Hypothesis Testing

The maximum likelihood analysis framework presented in Younk et al. (2016) is used to analyze the maps. The test statistic is defined using the likelihood ratio,

$$TS = 2 \ln \frac{\mathcal{L}^{\text{max}}(\text{Source Model})}{\mathcal{L}(\text{Null Model})}, \quad (1)$$

to compare a source model hypothesis with a null hypothesis. The likelihood of a model $\mathcal{L}(\text{Model})$ is ob-

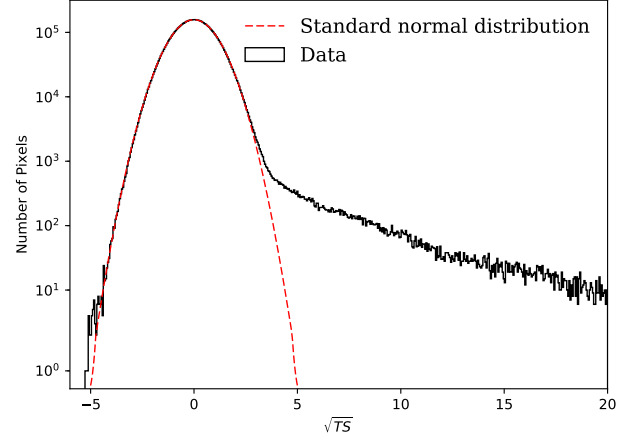


Figure 2. Test statistic distribution of the point source search (black) and standard normal distribution (red).

tained by comparing the observed event counts with the expected counts, for all the pixels in a region of interest, and for all nine analysis bins.

For the null model, the expected counts are simply given by the background maps derived from data. For the source model, the expected counts correspond to the same background plus a signal contribution from the source derived from simulation. We assume a source model characterized by:

- a point source or a uniform disk of fixed radius and
- a power law energy spectrum.

The signal contribution is derived from the source characteristics and the detector response from simulation (expected counts for the spectrum and PSF, both functions of the analysis bin and the declination).

The TS is maximized with respect to the free parameters of the source model. This approach is used both to search for sources (with a TS threshold) and to measure the characteristics of said sources as a result of the maximization.

We make a TS map by moving the location of the hypothetical source across the possible locations in the sky. In the following searches the source flux is the only free parameter of the model while the extent and spectral index are fixed. The source and null model are nested; hence by Wilks' Theorem the TS is distributed as χ^2 with one degree of freedom if the statistics are sufficiently large. Consequently, the pre-trial significance, conventionally reported as standard deviations (sigmas), is obtained by taking the square root of the test statistic, \sqrt{TS} (here and after, what we denote \sqrt{TS} actually corresponds to $\text{sign}(TS) \sqrt{|TS|}$). Figure 2 shows the distri-

bution of $\sqrt{\text{TS}}$ across the sky for the point source search, as well as a standard normal distribution scaled by the number of pixels. For values lower than ~ 3 , the $\sqrt{\text{TS}}$ is well reproduced by the normal distribution, whereas at greater values a large excess can be seen due to the presence of sources in the sky.

3.5. Catalog Construction

In order to take advantage of HAWC's sensitivity to both pointlike and extended sources, multiple searches are conducted assuming either point or extended sources. The TS maps used for the search are computed using a source model consisting of a single test source with a fixed geometry (point source or uniform disk of fixed radius) and an energy spectrum consisting of a power law of fixed index,

$$dN/dE = F_0(E/E_0)^\alpha, \quad (2)$$

where E_0 is a reference energy, F_0 is the differential flux at E_0 and α is the spectral index.

For the known TeVCat sources that can be considered pointlike given the angular resolution of the HAWC instrument (i.e. the TeVCat extent is of the order of the PSF size or smaller), the spectral indices measured by HAWC vary around -2.7 , from approximately -3.1 to -2.5 , and are typically softer than the indices listed in TeVCat. This can be explained if the sources soften or cut off at the energies observed by HAWC. On the other hand, the Geminga PWN, which was first observed at TeV energies by the Milagro collaboration (Abdo et al. 2009), is detected by HAWC with an extent of about 2° and a hard spectral index around -2 . To account for the range of source extents and spectra observed with HAWC, four different maps were used to build the catalog, testing various source hypotheses. In order to limit computing time, the resolutions of the maps are adapted to the characteristic dimension of the hypothetical source, without significantly affecting the results:

1. A point source map of index -2.7 (HEALPix map resolution $N_{\text{side}} = 1024$ or 0.06° per pixel).
2. An extended source map of radius 0.5° and index -2.0 ($N_{\text{side}} = 512$ or 0.1° per pixel).
3. An extended source map of radius 1.0° and index -2.0 ($N_{\text{side}} = 256$ or 0.2° per pixel).
4. An extended source map of radius 2.0° and index -2.0 ($N_{\text{side}} = 256$ or 0.2° per pixel).

When building the catalog, the priority is given to the point source search, then the extended searches ordered

by increasing radius. This limits possible source contamination when multiple nearby sources are added together. However, a strong extended source may be found in the point source search, possibly multiple times (see e.g. Geminga below), as well as in the extended search. Hence, the exact search in which a source is first tagged is not a perfect indication of the source extent. More robust morphology studies will be performed in a future analysis and are beyond the scope of this catalog paper.

To select the sources in the maps, all local maxima with $\text{TS} > 25$ are flagged. In some regions, multiple local maxima are found very near each other. We define as primary sources all local maxima that are separated from neighboring local maxima of higher significance by a valley of $\Delta(\sqrt{\text{TS}}) > 2$. We also define and include secondary sources when $1 < \Delta(\sqrt{\text{TS}}) < 2$. These sources are marked with an asterisk (*).

The final catalog comprises the sources of the point source search plus the sources of the extended searches, ordered by increasing radius, if their locations are more than 2° away from any hotspot with TS greater than 25 in the previous searches.

3.6. False Positive Expectation

When selecting the sources in the map, a background fluctuation can sometimes mimic a source and fulfill the selection criteria. To estimate this possible contamination, the search was run on randomized background maps. Events maps are generated for each of the nine analysis bins, and then the full search strategy as for the data map is employed, including point and extended source searches, as detailed on Section 3.5. This complete procedure was run with 20 sets of simulated maps. In 11 cases, no sources were flagged. In 9 cases, one source was flagged. In total, out of the 20 full searches performed over the entire sky, 9 sources were flagged, so the predicted number of background fluctuations passing the $\text{TS} > 25$ criterion is about $9/20 = 0.45$. Therefore, the predicted number of false positive in the catalog is about 0.5. These possible fluctuations are typically close to the threshold value $\text{TS} = 25$ and are usually out of the Galactic Plane, as it only represents a small fraction of the visible sky.

3.7. Source Position, Extent, and Energy Spectrum

The source positions reported in this catalog correspond to the first search in which they appear, as presented in Section 3.5. The statistical uncertainty of the position is defined as the maximum distance between the center and the 1-sigma contour obtained from the TS map.

After the search, a residual map is generated and halo-like structures are visible around several sources mod-

eled as point sources. This halo is used to define a tentative source radius for the secondary source model when fitting the energy spectrum (results presented in Table 3 of the next section). This radius should not be regarded as a definite measurement of the source extent but can nonetheless provide useful information on how much the spectrum measurement depends on the source region definition. When this new source region definition is a good representation of the actual source, the newly fitted spectrum should better correspond to the source spectrum, however as it corresponds to a larger region it is more subject to contamination from other sources or possibly diffuse emission. Additionally, for some complex regions, or regions for which independent analyses are performed, the whole region is fit, explicitly including multiple sources, as an estimate of the total flux of the region. Such regions are discussed in Section 5.

Once the source location and size are defined, the source spectrum is fit using a power law (Equation 2). For the range of declinations considered, the reference energy of 7 TeV minimizes the correlation between the index and normalization, energy which corresponds to the region of maximum sensitivity (cf. Figure 3, right). We report the differential flux at 7 TeV (F_7), the index α , and the statistical uncertainties on both parameters in Table 3.

3.8. Diffuse Galactic emission

At GeV energies, diffuse emission resulting from the interaction of cosmic rays with matter and photons is the dominant component of the gamma-ray sky. This diffuse emission has a steeper spectrum than galactic gamma-ray sources and as a result the TeV sky is source dominated. The Milagro and H.E.S.S. experiments measured the TeV diffuse emission in [Abdo et al. \(2008\)](#) and [Abramowski et al. \(2014\)](#). Both measured a higher flux than predicted – by the numerical cosmic-ray propagation code GALPROP ([Strong et al. 2007](#)) for Milagro¹, and a hadronic model for H.E.S.S.–, likely due to unresolved sources. A diffuse emission is not included in the likelihood model used in the present analysis. We are concerned that sources identified by this analysis may have a significant underlying diffuse component, or in extreme cases arise from background fluctuations in a continuous region of diffuse emission. To estimate the maximum possible contribution of the diffuse emission to the spectrum measurement, we simulate a uniform flux with a normalization corresponding to the peak

¹ The conventional GALPROP version here, since the optimized version was derived to fit the EGRET excess which was latter refuted by *Fermi*-LAT.

flux value of the hadronic model reported by H.E.S.S. ($1 \times 10^{-9} \text{ TeV}^{-1} \text{ cm}^{-2} \text{ s}^{-1} \text{ sr}^{-1}$ at 1 TeV) and a spectral index of -2.7 . We estimate that, for the low latitude sources near the detection threshold (where the diffuse contribution will be the largest), the diffuse emission can contribute to $<30\%$ of the fluxes measured with the point source hypothesis.

As an alternative method of estimating the contribution from Galactic Diffuse emission, we can use a region of the Galactic Plane with no detected sources to derive a conservative upper limit on this contribution. As with the analyses by HESS and Milagro mentioned above, this approach will naturally overestimate the diffuse component since it includes unresolved sources. We use the region with longitude l between 56° and 64° and latitude $|b| < 0.5^\circ$, which does not contain detected sources. The median differential flux at 7 TeV measured in this region with the point source model is $2.1 \times 10^{-15} \text{ TeV}^{-1} \text{ cm}^{-2} \text{ s}^{-1}$. This small excess over a large region indicates the presence of either the Galactic diffuse emission, some unresolved sources, or more likely a combination of both. We use it as an upper limit to estimate the impact of the diffuse on the flux of the sources measured in the plane near $l = 60^\circ$. We extrapolate to lower latitudes using the shape of the longitudinal profile of the diffuse emission from GALPROP in [Abdo et al. \(2008\)](#). We find that in this approach the diffuse emission can contribute up to 60% of the flux measurement of the weak, low-latitude sources (TS close to 25), that have longitudes between 34° and 50° . For $l > 50^\circ$ the modeled diffuse emission is lower, and for $l < 34^\circ$ all the detected sources have higher fluxes and they are not impacted significantly by the diffuse emission. The sources for which this conservative estimate is above 30% of the measured point source flux at 7 TeV are 2HWC J1852+013*, 2HWC J1902+048*, 2HWC J1907+084*, 2HWC J1914+117*, 2HWC J1921+131, and 2HWC J1922+140; as defined and discussed in Sections 4 and 5. In the likely case in which part or most of the flux measured in the $l = [56^\circ, 64^\circ]$ region indeed contains unresolved sources, the diffuse flux is lesser and so is its contribution of the flux reported on this catalog.

Future dedicated analysis of the HAWC data will allow to better constrain the Galactic diffuse emission.

3.9. Systematic Uncertainties

The absolute pointing of the HAWC Observatory is initially determined using a careful survey of the WCDs and PMTs and then refined using the observed position of the Crab Nebula. The positions of Markarian 421 and Markarian 501 are observed by HAWC within 0.05° of their known locations after the pointing calibration.

Additional studies based on the observation of the Crab Nebula when it is farther from zenith showed that absolute pointing is still better than 0.1° up to a zenith angle of 45° , which covers the full declination range considered in the present study. Therefore the systematic uncertainty on the absolute pointing of the catalog is quoted as 0.1° .

For isolated point sources, the systematic uncertainties on the spectrum measurement are estimated to be $\pm 50\%$ for the overall flux and ± 0.2 for the spectral index (Abeysekara et al. 2017, submitted to ApJ). In the present analysis, no detailed morphology study is performed. However, there is a correlation between the assumed source size and the measured spectrum. Simulation studies show that for isolated sources the unknown extent can induce an additional systematic uncertainty on the spectral index measurement of up to 0.3.

As we test the presence of a single source at a time without modeling the other sources, the likelihood computation may be impacted by events from a neighboring source. This is true in particular for the lower energy events where the PSF is wider. By adding events to the single hypothesized source, this contamination can increase the measured flux and make the spectral index softer. In the case of two identical point sources located 1° apart, the flux measurement, assuming a known spectral index, is increased by 20% to 30%, depending on the declination. When fitting the index as well, the index can change by up to 0.1 and the measured flux is changed by about 20% to 40%. This confusion is considered a systematic uncertainty of the present analysis and tends to be larger in the very populated regions of the sky with high source population.

4. RESULTS

We present the result of the search, the 2HWC catalog. A total of 39 sources are found², 4 of which are detected with the extended search procedure only. As discussed in Section 3.6, the predicted number of background fluctuations passing the selection criteria is about 0.5. Out of these 39 sources, 16 are more than a degree away from known TeV sources listed in TeVCat.

4.1. HAWC Performance

Due to the development of air showers in the atmosphere, HAWC's sensitivity as well as energy response varies with the source declination. The sensitivity of the point source search is represented in Figure 3, left. The curves correspond to the flux that gives a central expectation of a 5σ signal for a point source with a power law

flux of index -2.0 , -2.5 , and -3.0 . The maximum sensitivity is obtained for sources transiting at the zenith of HAWC, i.e. whose declinations are close to 19° . The sources found in the point source search are also represented here: the measured flux and statistical uncertainty are shown at the corresponding declination.

The energy range that contributes to most of the test statistic in the point source search, derived from simulation, is represented in Figure 3, right. More precisely, assuming a given spectral model, we show the energy range as the energy defining the central 75% of the contribution to the test statistic. Three spectral models are represented: power laws of index -2.0 , -2.5 , and -3.0 . For a given spectral model, the energy range that contributes most of the test statistic shifts to lower values for sources transiting overhead than for sources whose declinations are far from 19° .

4.2. Maps

The test-statistic map derived from the all-sky search for point sources with index -2.7 is presented in equatorial coordinates in Figure 4. The inner Galactic Plane is clearly visible. In the outer Galactic Plane, the Crab and Geminga are visible. Outside of the Galactic Plane, Markarian 421 and Markarian 501 stand out.

Figures 5 to 9 show detailed views of smaller regions of the sky. 2HWC sources are represented by white circles and labels below the circle. The source locations listed in TeVCat are also marked, with black squares and labels above the square symbol.

The maps of the regions around the Crab, Markarian 421, and Markarian 501 are shown in Figure 5. The region of the outer Galactic Plane around Geminga is mapped in Figure 6. The left map shows the result of the point source search; the right map that of the 2° extended search. The increased TS in the extended search supports the case of a significant extent of the two TeV sources detected by the HAWC Observatory in this region. Isolated sources found out of the Galactic Plane are shown on Figure 7. Finally, the inner Galactic Plane from the Cygnus region towards the center of the Galaxy is shown in Figures 8 and 9.

4.3. Catalog

Table 2 lists all sources found using the procedure described in Section 3.5, ordered by right ascension. The first column lists the HAWC catalog name. The second column specifies the search in which the source first appeared with a TS above the threshold value of 25. PS denotes the point source search, 0.5, 1, and 2° the radius of the disk in the extended search. The corresponding TS value is reported in the third column. The

² Geminga is flagged twice but only counted as one here.

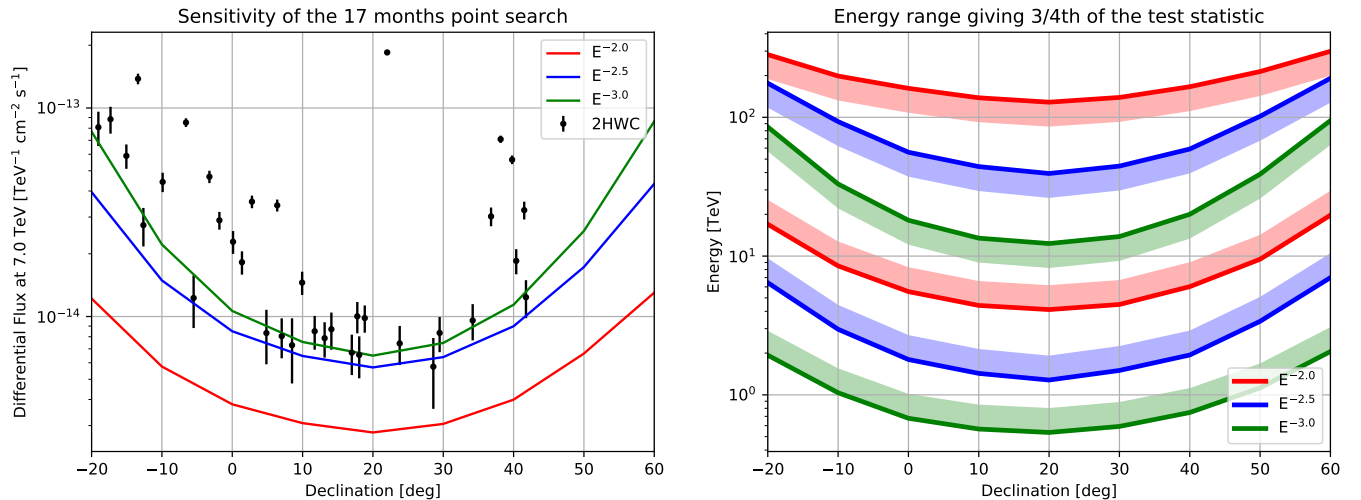


Figure 3. *Left:* Sensitivity of the point source search for three spectral hypotheses, as a function of declination. We show the flux required to give a central expectation of 5σ , for the present analysis. The differential fluxes of the sources detected in the point source search are also shown with their statistical uncertainties. *Right:* Upper and lower ends of the energy range contributing to the central 3 quarters of the test statistic of the point source search, see text.

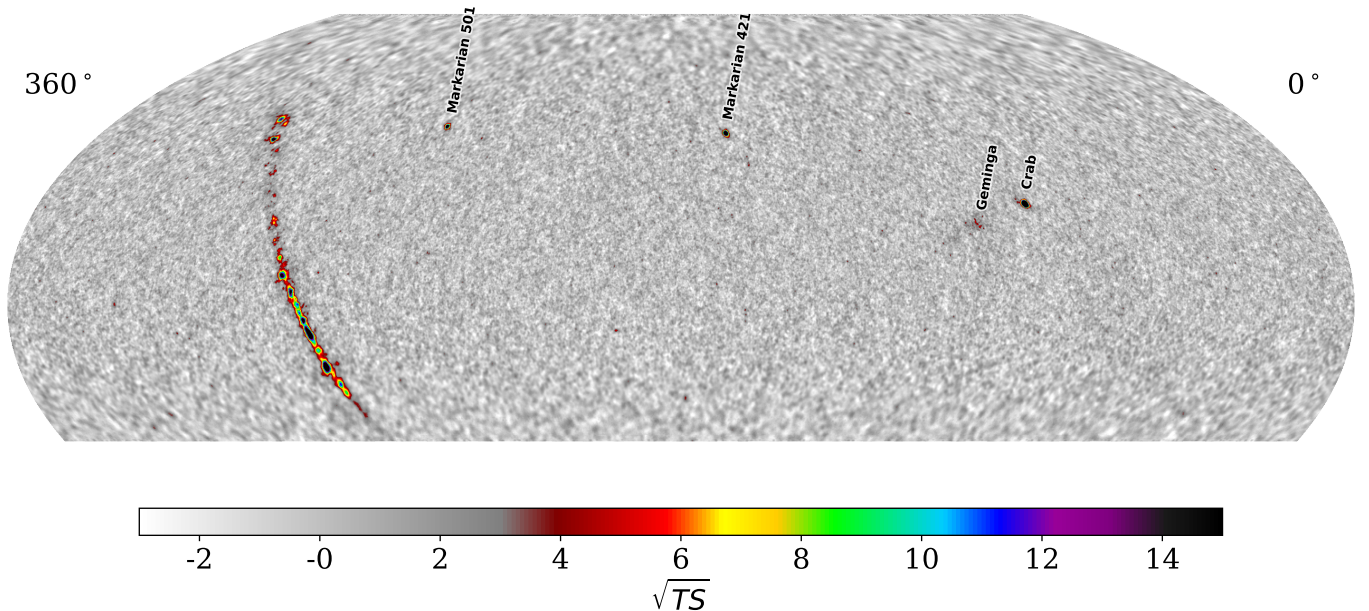


Figure 4. Equatorial full-sky TS map, for a point source hypothesis with a spectral index of -2.7 .

following columns compile the source positions in equatorial (J2000.0 epoch) and Galactic coordinates and the one-sigma uncertainty on the position of the maximum identified in the respective search. The second part of the table, after the vertical line, provides information on the nearest TeVCat source: the distance, then the corresponding name if this distance is less than 1° .

Table 3 lists the differential photon flux at 7 TeV (F_7) and the spectral index of the power law that fit the

source identified in HAWC data best. For all sources we report the flux estimated with the source model corresponding to the search in which the source was found. For the sources for which an additional source size hypothesis was defined, as detailed in Section 3.7, the second flux measurement is also reported.

The results of Table 3 are illustrated in Figure 10. For fluxes $F_7 > 3 \times 10^{-14} \text{TeV}^{-1} \text{cm}^{-2} \text{s}^{-1}$ all sources have previously been detected using other instruments, but

Table 2. 2HWC source list and nearest TeVCat sources. The sources with a * symbol correspond to sources that are not separated from their neighbor by a large TS gap, as defined in section 3.5.

| Name | Search | TS | RA | Dec | l | b | 1σ stat. unc. | Nearest TeVCat source | |
|-----------------|----------------|---------|----------------|----------------|----------------|----------------|----------------------|-----------------------|-----------------|
| | | | | | | | | Dist. | Name |
| | | | [$^{\circ}$] | [$^{\circ}$] | [$^{\circ}$] | [$^{\circ}$] | [$^{\circ}$] | [$^{\circ}$] | |
| 2HWC J0534+220 | PS | 1.1E+4 | 83.63 | 22.02 | 184.55 | -5.78 | 0.06 | 0.01 | Crab |
| 2HWC J0631+169 | PS | 29.6 | 98.00 | 17.00 | 195.61 | 3.51 | 0.11 | 0.39 | Geminga |
| 2HWC J0635+180 | PS | 27.4 | 98.83 | 18.05 | 195.04 | 4.70 | 0.13 | 0.97 | Geminga |
| 2HWC J0700+143 | 1.0 $^{\circ}$ | 29 | 105.12 | 14.32 | 201.10 | 8.44 | 0.80 | 2.98 | - |
| 2HWC J0819+157 | 0.5 $^{\circ}$ | 30.7 | 124.98 | 15.79 | 208.00 | 26.52 | 0.17 | 7.86 | - |
| 2HWC J1040+308 | 0.5 $^{\circ}$ | 26.3 | 160.22 | 30.87 | 197.59 | 61.31 | 0.22 | 8.77 | - |
| 2HWC J1104+381 | PS | 1.15E+3 | 166.11 | 38.16 | 179.95 | 65.05 | 0.06 | 0.04 | Markarian 421 |
| 2HWC J1309-054 | PS | 25.3 | 197.31 | -5.49 | 311.11 | 57.10 | 0.22 | 3.27 | - |
| 2HWC J1653+397 | PS | 556 | 253.48 | 39.79 | 63.64 | 38.85 | 0.07 | 0.03 | Markarian 501 |
| 2HWC J1809-190 | PS | 85.5 | 272.46 | -19.04 | 11.33 | 0.18 | 0.17 | 0.31 | HESS J1809-193 |
| 2HWC J1812-126 | PS | 26.8 | 273.21 | -12.64 | 17.29 | 2.63 | 0.19 | 0.14 | HESS J1813-126 |
| 2HWC J1814-173 | PS | 141 | 273.52 | -17.31 | 13.33 | 0.13 | 0.18 | 0.54 | HESS J1813-178 |
| 2HWC J1819-150* | PS | 62.9 | 274.83 | -15.06 | 15.91 | 0.09 | 0.16 | 0.51 | SNR G015.4+00.1 |
| 2HWC J1825-134 | PS | 767 | 276.46 | -13.40 | 18.12 | -0.53 | 0.09 | 0.39 | HESS J1826-130 |
| 2HWC J1829+070 | PS | 25.3 | 277.34 | 7.03 | 36.72 | 8.09 | 0.10 | 8.12 | - |
| 2HWC J1831-098 | PS | 107 | 277.87 | -9.90 | 21.86 | -0.12 | 0.17 | 0.01 | HESS J1831-098 |
| 2HWC J1837-065 | PS | 549 | 279.36 | -6.58 | 25.48 | 0.10 | 0.06 | 0.37 | HESS J1837-069 |
| 2HWC J1844-032 | PS | 309 | 281.07 | -3.25 | 29.23 | 0.11 | 0.10 | 0.18 | HESS J1844-030 |
| 2HWC J1847-018 | PS | 132 | 281.95 | -1.83 | 30.89 | -0.03 | 0.11 | 0.17 | HESS J1848-018 |
| 2HWC J1849+001 | PS | 134 | 282.39 | 0.11 | 32.82 | 0.47 | 0.10 | 0.16 | IGR J18490-0000 |
| 2HWC J1852+013* | PS | 71.4 | 283.01 | 1.38 | 34.23 | 0.50 | 0.13 | 1.37 | - |
| 2HWC J1857+027 | PS | 303 | 284.33 | 2.80 | 36.09 | -0.03 | 0.06 | 0.14 | HESS J1857+026 |
| 2HWC J1902+048* | PS | 31.7 | 285.51 | 4.86 | 38.46 | -0.14 | 0.18 | 2.03 | - |
| 2HWC J1907+084* | PS | 33.1 | 286.79 | 8.50 | 42.28 | 0.41 | 0.27 | 1.15 | - |
| 2HWC J1908+063 | PS | 367 | 287.05 | 6.39 | 40.53 | -0.80 | 0.06 | 0.14 | MGRO J1908+06 |
| 2HWC J1912+099 | PS | 83.2 | 288.11 | 9.93 | 44.15 | -0.08 | 0.10 | 0.24 | HESS J1912+101 |
| 2HWC J1914+117* | PS | 33 | 288.68 | 11.72 | 46.00 | 0.25 | 0.13 | 1.64 | - |
| 2HWC J1921+131 | PS | 30.1 | 290.30 | 13.13 | 47.99 | -0.50 | 0.12 | 1.14 | - |
| 2HWC J1922+140 | PS | 49 | 290.70 | 14.09 | 49.01 | -0.38 | 0.11 | 0.10 | W 51 |
| 2HWC J1928+177 | PS | 65.7 | 292.15 | 17.78 | 52.92 | 0.14 | 0.07 | 1.18 | - |
| 2HWC J1930+188 | PS | 51.8 | 292.63 | 18.84 | 54.07 | 0.24 | 0.12 | 0.03 | SNR G054.1+00.3 |
| 2HWC J1938+238 | PS | 30.5 | 294.74 | 23.81 | 59.37 | 0.94 | 0.13 | 2.75 | - |
| 2HWC J1949+244 | 1.0 $^{\circ}$ | 34.9 | 297.42 | 24.46 | 61.16 | -0.85 | 0.71 | 3.43 | - |
| 2HWC J1953+294 | PS | 30.1 | 298.26 | 29.48 | 65.86 | 1.07 | 0.24 | 8.44 | - |
| 2HWC J1955+285 | PS | 25.4 | 298.83 | 28.59 | 65.35 | 0.18 | 0.14 | 7.73 | - |
| 2HWC J2006+341 | PS | 36.9 | 301.55 | 34.18 | 71.33 | 1.16 | 0.13 | 3.61 | - |
| 2HWC J2019+367 | PS | 390 | 304.94 | 36.80 | 75.02 | 0.30 | 0.09 | 0.07 | VER J2019+368 |
| 2HWC J2020+403 | PS | 59.7 | 305.16 | 40.37 | 78.07 | 2.19 | 0.11 | 0.40 | VER J2019+407 |
| 2HWC J2024+417* | PS | 28.4 | 306.04 | 41.76 | 79.59 | 2.43 | 0.20 | 0.97 | MGRO J2031+41 |
| 2HWC J2031+415 | PS | 209 | 307.93 | 41.51 | 80.21 | 1.14 | 0.09 | 0.08 | TeV J2032+4130 |

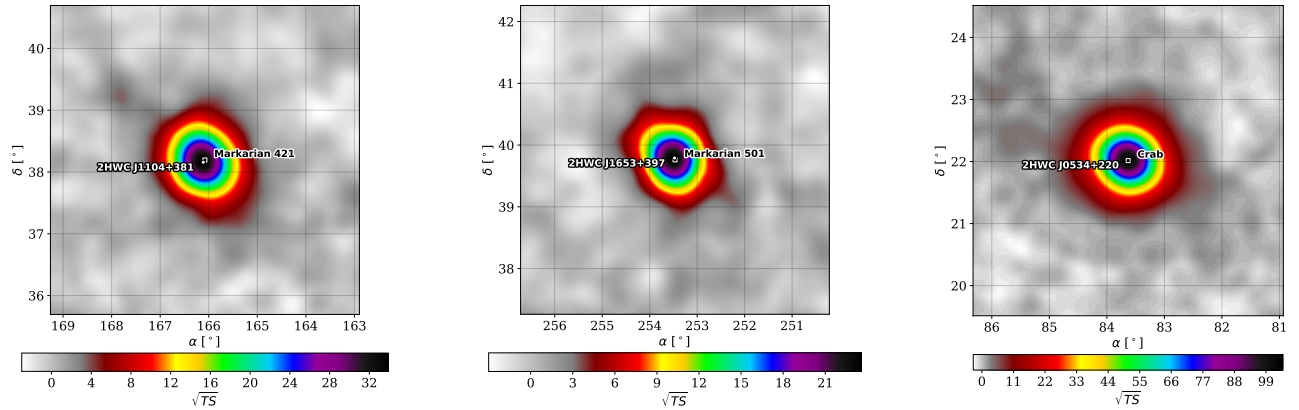


Figure 5. Regions around Markarian 421, Markarian 501, and the Crab Nebula: Equatorial TS maps, for a point source hypothesis with a spectral index of -2.7 . In this figure and the followings, the 2HWC sources are represented by white circles and labels below the circle; whereas the source listed in TeVCat are represented with black squares and labels above the square symbol.

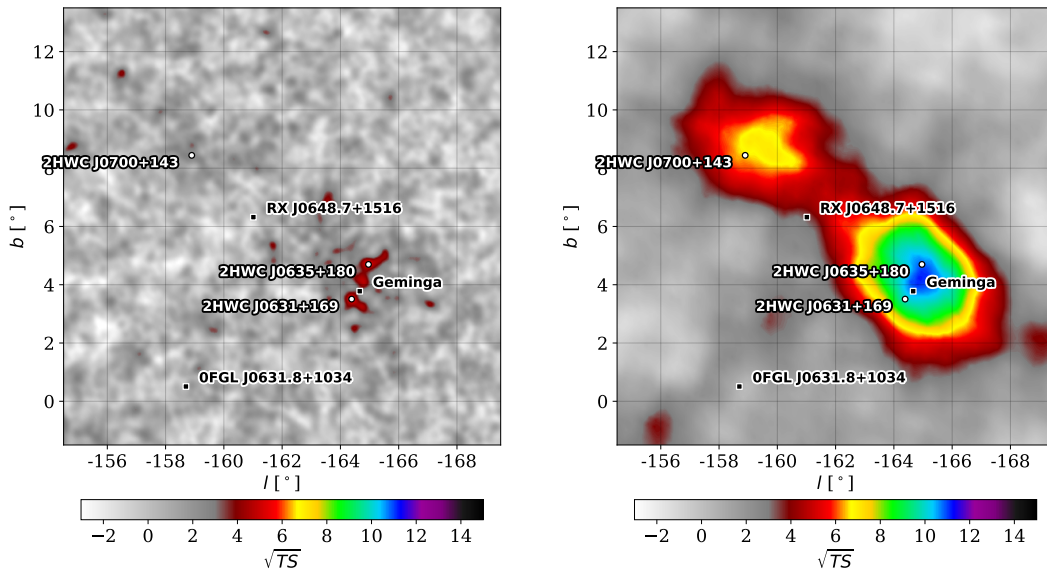


Figure 6. Region around Geminga, in Galactic coordinates. Left: TS map for a point source hypothesis with a spectral index of -2.7 . Right: TS map for an extended source hypothesis represented by a disk of radius of 2.0 degrees with a spectral index of -2.0 .

Table 3. The 2HWC catalog: Source radius, fitted spectrum, and TeV counterpart. The flux F_7 is the differential flux at 7 TeV. For some sources an additional line indicates another spectral fit with a more extended source assumption. The uncertainties reported here are statistical only. The systematic uncertainties are 0.1° for the position, 50% for the flux, and 0.2 for the index.

| Name | Tested radius [$^\circ$] | Index | $F_7 \times 10^{15}$ [$\text{TeV}^{-1} \text{cm}^{-2} \text{s}^{-1}$] | TeVCat |
|-----------------|-------------------------------|------------------|--|-----------------|
| 2HWC J0534+220 | - | -2.58 ± 0.01 | 184.7 ± 2.4 | Crab |
| 2HWC J0631+169 | - | -2.57 ± 0.15 | 6.7 ± 1.5 | Geminga |
| " | 2.0 | -2.23 ± 0.08 | 48.7 ± 6.9 | Geminga |
| 2HWC J0635+180 | - | -2.56 ± 0.16 | 6.5 ± 1.5 | Geminga |
| 2HWC J0700+143 | 1.0 | -2.17 ± 0.16 | 13.8 ± 4.2 | - |
| " | 2.0 | -2.03 ± 0.14 | 23.0 ± 7.3 | - |
| 2HWC J0819+157 | 0.5 | -1.50 ± 0.67 | 1.6 ± 3.1 | - |
| 2HWC J1040+308 | 0.5 | -2.08 ± 0.25 | 6.6 ± 3.5 | - |
| 2HWC J1104+381 | - | -3.04 ± 0.03 | 70.8 ± 2.9 | Markarian 421 |
| 2HWC J1309-054 | - | -2.55 ± 0.18 | 12.3 ± 3.5 | - |
| 2HWC J1653+397 | - | -2.86 ± 0.04 | 56.5 ± 2.7 | Markarian 501 |
| 2HWC J1809-190 | - | -2.61 ± 0.11 | 80.9 ± 15.1 | HESS J1809-193 |
| 2HWC J1812-126 | - | -2.84 ± 0.16 | 27.4 ± 5.7 | HESS J1813-126 |
| 2HWC J1814-173 | - | -2.61 ± 0.09 | 88.4 ± 13.0 | HESS J1813-178 |
| " | 1.0 | -2.55 ± 0.07 | 151.6 ± 18.8 | HESS J1813-178 |
| 2HWC J1819-150* | - | -2.88 ± 0.10 | 59.0 ± 7.9 | SNR G015.4+00.1 |
| 2HWC J1825-134 | - | -2.58 ± 0.04 | 138.0 ± 8.1 | HESS J1826-130 |
| " | 0.9 | -2.56 ± 0.03 | 249.2 ± 11.4 | HESS J1826-130 |
| 2HWC J1829+070 | - | -2.69 ± 0.17 | 8.1 ± 1.7 | - |
| 2HWC J1831-098 | - | -2.80 ± 0.09 | 44.2 ± 4.7 | HESS J1831-098 |
| " | 0.9 | -2.64 ± 0.06 | 95.8 ± 8.0 | HESS J1831-098 |
| 2HWC J1837-065 | - | -2.90 ± 0.04 | 85.2 ± 4.1 | HESS J1837-069 |
| " | 2.0 | -2.66 ± 0.03 | 341.3 ± 11.3 | HESS J1837-069 |
| 2HWC J1844-032 | - | -2.64 ± 0.06 | 46.8 ± 3.2 | HESS J1844-030 |
| " | 0.6 | -2.51 ± 0.04 | 92.8 ± 5.2 | HESS J1844-030 |
| 2HWC J1847-018 | - | -2.95 ± 0.08 | 28.9 ± 2.8 | HESS J1848-018 |
| 2HWC J1849+001 | - | -2.54 ± 0.10 | 22.8 ± 2.9 | IGR J18490-0000 |
| " | 0.8 | -2.47 ± 0.05 | 60.8 ± 4.5 | IGR J18490-0000 |
| 2HWC J1852+013* | - | -2.90 ± 0.10 | 18.2 ± 2.3 | - |
| 2HWC J1857+027 | - | -2.93 ± 0.05 | 35.5 ± 2.5 | HESS J1857+026 |
| " | 0.9 | -2.61 ± 0.04 | 97.3 ± 4.4 | HESS J1857+026 |
| 2HWC J1902+048* | - | -3.22 ± 0.16 | 8.3 ± 2.4 | - |
| 2HWC J1907+084* | - | -3.25 ± 0.18 | 7.3 ± 2.5 | - |
| 2HWC J1908+063 | - | -2.52 ± 0.05 | 34.1 ± 2.2 | MGRO J1908+06 |
| " | 0.8 | -2.33 ± 0.03 | 85.1 ± 4.2 | MGRO J1908+06 |
| 2HWC J1912+099 | - | -2.93 ± 0.09 | 14.5 ± 1.9 | HESS J1912+101 |
| " | 0.7 | -2.64 ± 0.06 | 36.6 ± 3.0 | HESS J1912+101 |
| 2HWC J1914+117* | - | -2.83 ± 0.15 | 8.5 ± 1.6 | - |
| 2HWC J1921+131 | - | -2.75 ± 0.15 | 7.9 ± 1.5 | - |
| 2HWC J1922+140 | - | -2.49 ± 0.15 | 8.7 ± 1.8 | W 51 |
| " | 0.9 | -2.51 ± 0.09 | 26.1 ± 3.4 | W 51 |
| 2HWC J1928+177 | - | -2.56 ± 0.14 | 10.0 ± 1.7 | - |
| 2HWC J1930+188 | - | -2.74 ± 0.12 | 9.8 ± 1.5 | SNR G054.1+00.3 |
| 2HWC J1938+238 | - | -2.96 ± 0.15 | 7.4 ± 1.6 | - |
| 2HWC J1949+244 | 1.0 | -2.38 ± 0.16 | 19.4 ± 4.2 | - |
| 2HWC J1953+294 | - | -2.78 ± 0.15 | 8.3 ± 1.6 | - |
| 2HWC J1955+285 | - | -2.40 ± 0.24 | 5.7 ± 2.1 | - |
| 2HWC J2006+341 | - | -2.64 ± 0.15 | 9.6 ± 1.9 | - |
| " | 0.9 | -2.40 ± 0.11 | 24.5 ± 4.2 | - |
| 2HWC J2019+367 | - | -2.29 ± 0.06 | 30.2 ± 3.1 | VER J2019+368 |
| " | 0.7 | -2.24 ± 0.04 | 58.2 ± 4.6 | VER J2019+368 |
| 2HWC J2020+403 | - | -2.95 ± 0.10 | 18.5 ± 2.6 | VER J2019+407 |
| 2HWC J2024+417* | - | -2.74 ± 0.17 | 12.4 ± 2.6 | MGRO J2031+41 |
| 2HWC J2031+415 | - | -2.57 ± 0.07 | 32.4 ± 3.2 | TeV J2032+4130 |
| " | 0.7 | -2.52 ± 0.05 | 61.6 ± 4.4 | TeV J2032+4130 |

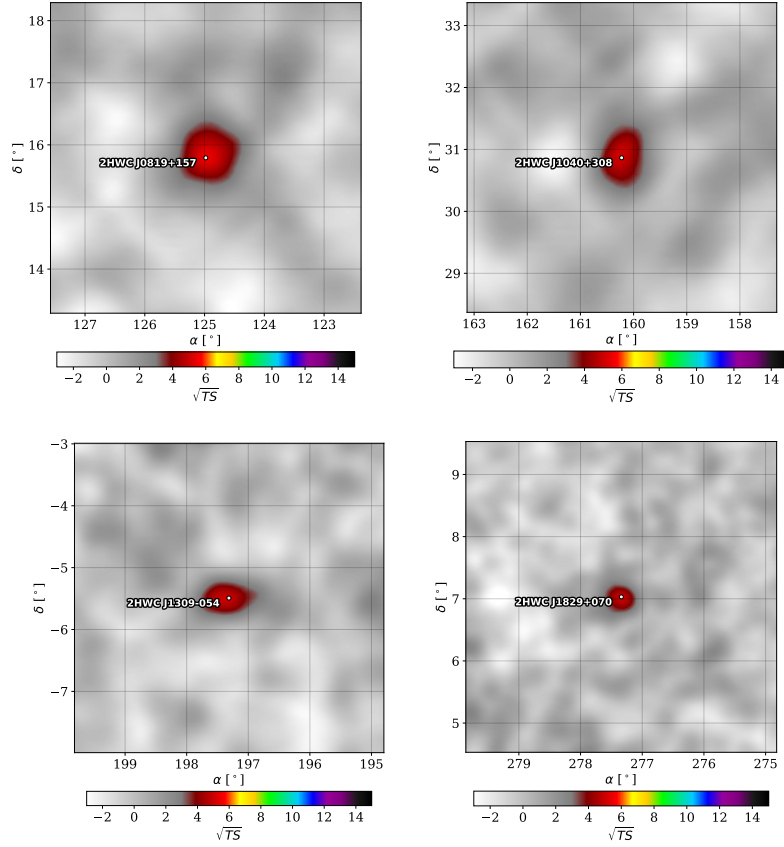


Figure 7. Regions around 2HWC J0819+157, 2HWC J1040+308, 2HWC J1309-054, and 2HWC J1829+070 in equatorial coordinates. The TS maps correspond to the search in which these sources were found: the extended source hypothesis with a radius of 0.5° and a spectral index of -2.0 for the former two, and the point source hypothesis and a spectral index of -2.7 for the latter two.

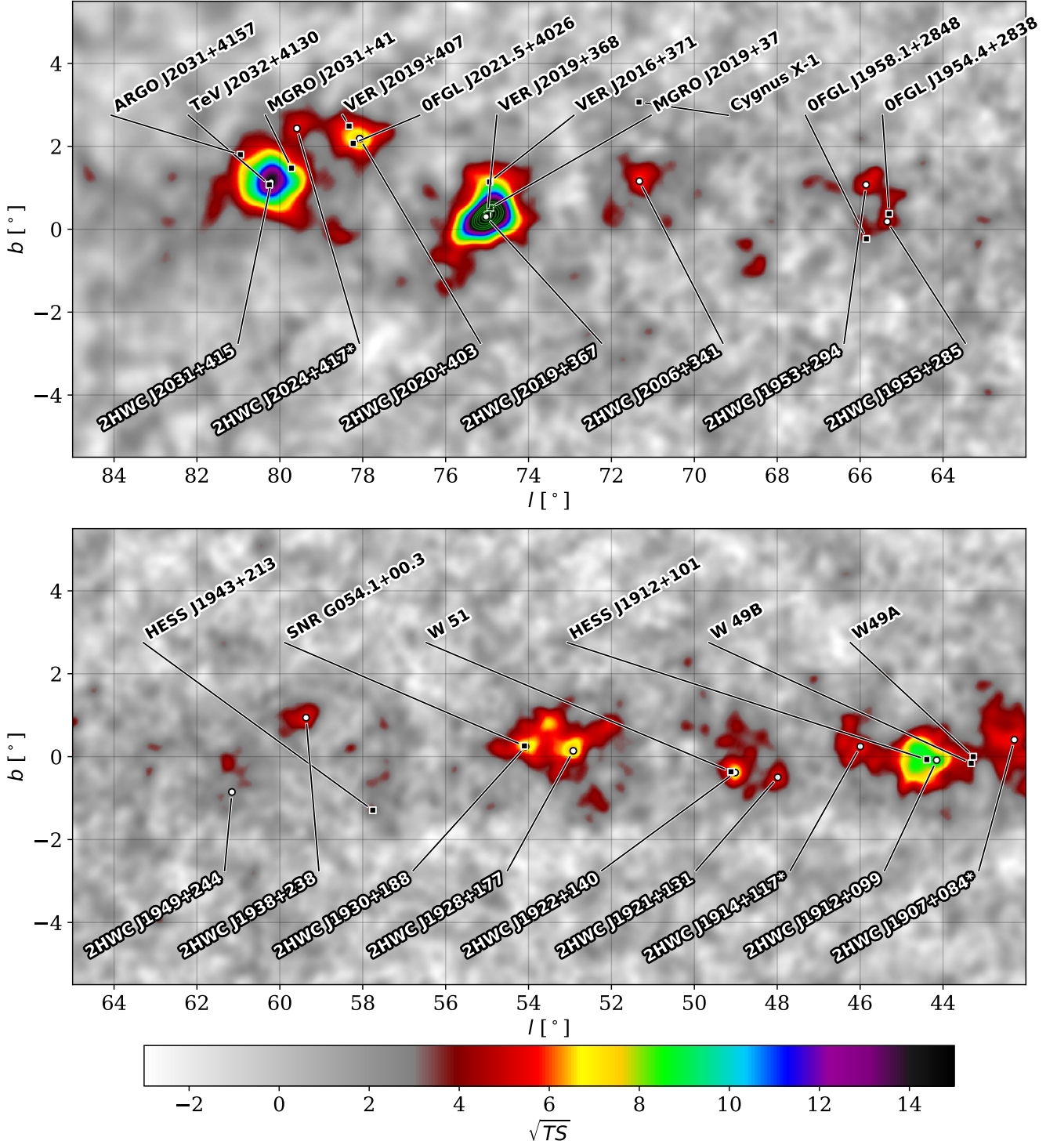


Figure 8. Parts of the inner Galactic Plane region, in Galactic coordinates. The TS map corresponds to a point source hypothesis with a spectral index of -2.7 . The green contour lines indicate values of \sqrt{TS} of 15, 16, 17, etc. In this figure and the following, the 2HWC sources are represented by white circles and labels below the circle; whereas the source listed in TeVCat are represented with black squares and labels above the square symbol.

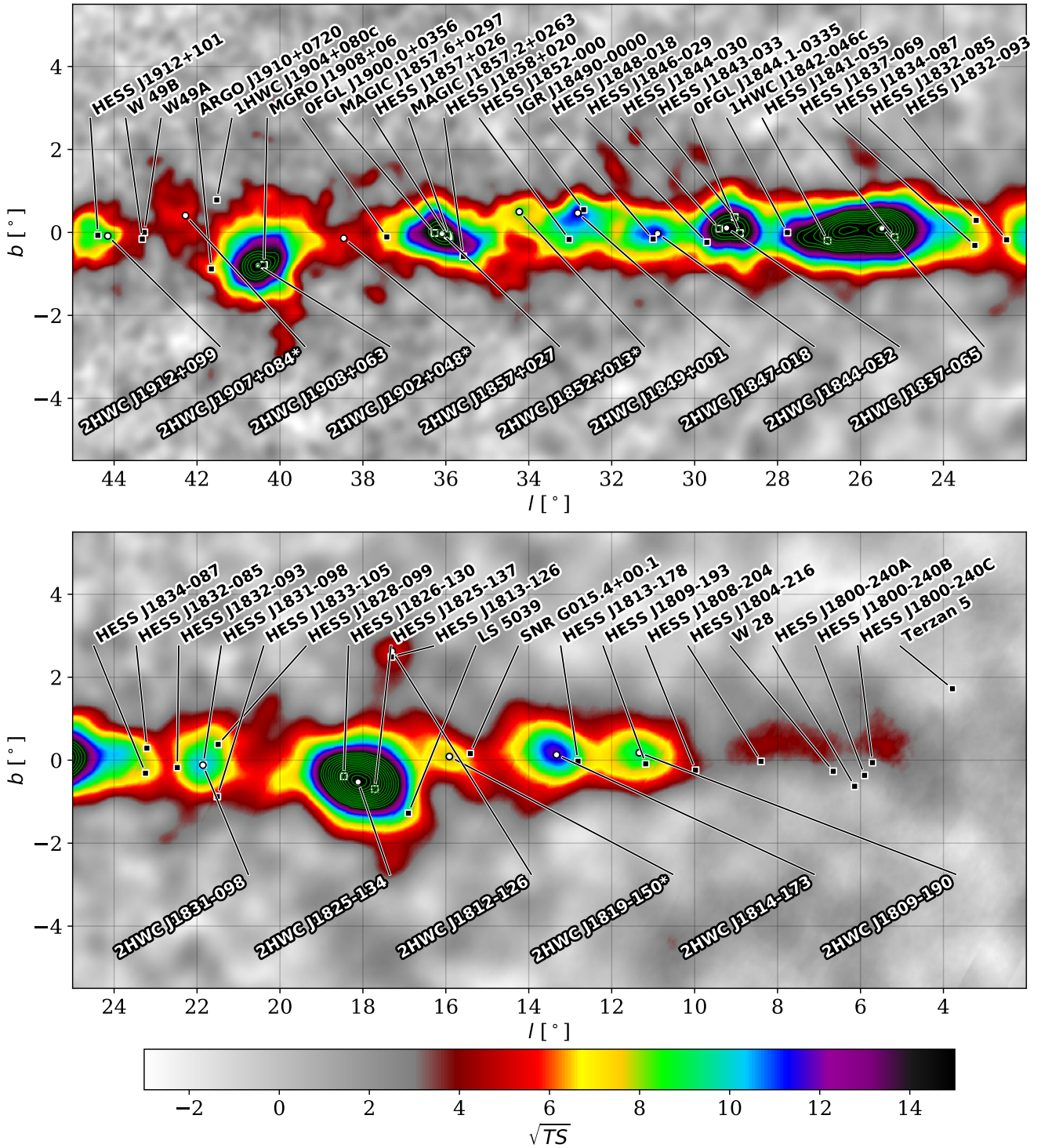


Figure 9. Same as Figure 8, farther along the Galactic Plane.

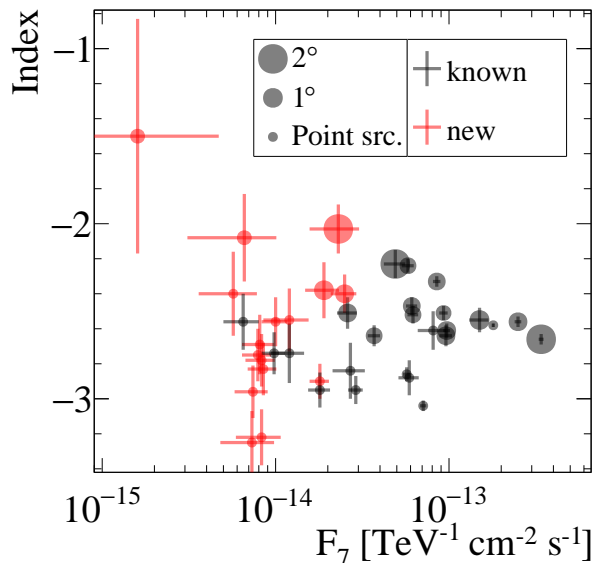


Figure 10. Distribution of the 2HWC sources in flux at 7 TeV (F_7) and power-law index. The marker size indicates the source extent to calculate the source flux and the color indicates whether these sources have (gray) or do not have (red) a counterpart in TeVCat.

below this value the fraction of newly detected sources dominates the sample. We note here that, when taking into account the full extent of each source, the Crab Nebula is only the third brightest source in the sky at 7 TeV. The brightest sources are 2HWC J1837-065 and 2HWC J1825-134.

In Figure 10 there is a region, around $F_7 = 0.8 \times 10^{-15} \text{ TeV}^{-1} \text{ cm}^{-2} \text{ s}^{-1}$ and power law index < -2.7 , where new catalog sources cluster. These sources do not have significant flux beyond the PSF of HAWC and should therefore provide interesting targets for follow-up with IACTs.

5. DISCUSSION

In this section we briefly discuss each source and its possible associations, ordered by right ascension. Of particular interest are the sources detected with previous and current TeV instruments, including the 1HWC sources observed in the inner Galaxy with a partial configuration of HAWC (Abeysekara et al. 2016) and sources listed in TeVCat. GeV counterparts are also searched in the *Fermi*-LAT catalogs: the standard 2FGL and 3FGL catalogs (Abdo et al. 2010a; Nolan et al. 2012; Acero et al. 2015), the high energy 1FHL and 2FHL catalogs (Ackermann et al. 2013, 2016), the second pulsar catalogs (Abdo et al. 2013), and the SNR catalog (Acero et al. 2016). The ATNF pulsar catalog (Manchester et al. 2005) is used to look for nearby pul-

sars. When available, the pulsars spindown power \dot{E} , distance d , and age τ are reported, as obtained from the ATNF catalog unless mentioned otherwise. Associations are typically search for within 0.5° of the position measured by HAWC.

5.1. 2HWC J0534+220 – Crab

2HWC J0534+220 is the source with the largest significance in this catalog, with $\text{TS} = 1.1 \times 10^4$. It corresponds to the Crab PWN, which is the first TeV source detected, in 1989 (Weekes et al. 1989), and which is since commonly used as a calibration source for TeV instruments. The associated pulsar is young and has a high spindown power ($\dot{E} = 4.5 \times 10^{38} \text{ erg s}^{-1}$, $d = 2.0 \text{ kpc}$, $\tau = 1.26 \text{ kyr}$). In the GeV regime, the emission is dominated by the pulsed emission originating from the pulsar. Although the pulsed emission has been observed up to 1.5 TeV (Ansoldi et al. 2016), most of the TeV emission is due to inverse Compton scattering in the surrounding PWN (Atoyan & Aharonian 1996).

The spectrum measured here matches previously published results. A more complete analysis of the Crab Nebula observation by HAWC will be presented in a separate publication (Abeysekara et al. 2017, submitted to ApJ).

5.2. 2HWC J0631+169 and 2HWC J0635+180 – Geminga

2HWC J0631+169 and 2HWC J0635+180 are both found in the point source search, each above the TS threshold value of 25. The corresponding TS maximum in the 2° extended search is 126. They appear to be associated with Geminga, a known GeV (Abdo et al. 2010b) gamma-ray pulsar. Prior to HAWC, Milagro was the only TeV instrument to have detected it. Milagro reported an extended source of full width at half maximum around 2.6° and a hard spectrum (Abdo et al. 2009). The large extent of the source makes it difficult for IACTs to observe it. To date none have reported a detection of Geminga (see e.g. Ahnen et al. (2016)).

Compared to other TeV PWNe, the associated pulsar PSR J0633+1746 is relatively old (342 kyr), nearby ($250_{-62}^{+120} \text{ pc}$) and has a low spindown power ($3.2 \times 10^{34} \text{ erg s}^{-1}$). Geminga (together with PSR B0656+14) has been proposed as the dominant source of the local population of TeV electrons and positrons, and thus a possible explanation for the PAMELA positron excess (Aharonian et al. 1995; Yüksel et al. 2009).

When fitted with a uniform disk source model, the extent observed in HAWC is around 2° in radius, and the measured spectral index is relatively hard at -2.2 . The measured spectrum depends on the assumed morphology. A detailed study of Geminga and 2HWC

J0700+143 (see next section) by HAWC will be presented in a dedicated publication (HAWC Collaboration 2017, in preparation).

5.3. 2HWC J0700+143

2HWC J0700+143 is a new TeV source discovered in the 1° extended search, with a TS of 29. The corresponding TS maximum in the 2° extended search is 51. It is likely associated with the B0656+14 pulsar, which has similar characteristics to the Geminga pulsar: old (111 kyr), nearby (288_{-27}^{+33} pc) and low spindown power (3.8×10^{34} erg s $^{-1}$) (Brisken et al. 2003). The associated supernova is believed to be the origin of the Monogem Ring. As for Geminga, PSR B0656+14 has been proposed as a significant contributor to the local lepton populations.

The measured extent of this source is around 2° , with a hard spectral index of about -2 .

5.4. 2HWC J0819+157

This source is found in the 0.5° radius extended search, with a TS value of 30.7. The coordinates correspond to a location out of the Galactic Plane ($b = 26.52^\circ$). The fitted index (-1.50) is much harder than the fitted index of any other source. The nearest potentially high energy source is the AGN 2MASS J08203478+1531114, 0.3 away. However, its distance ($z = 0.14$) seems incompatible with the observed extent and hard spectrum.

5.5. 2HWC J1040+308

Similar to 2HWC J0819+157, this source is found in the 0.5° radius extended search, with a TS value of 26.3. No obvious associations are found in the catalogs. The coordinates correspond to a location out of the Galactic Plane ($b = 61.31^\circ$), which seems in tension with the source extent.

5.6. 2HWC J1104+381 and 2HWC J1653+397 – Markarian 421 and Markarian 501

Markarian (Mrk) 421 and Mrk 501 are two of the closest and brightest extragalactic sources in the TeV as well as the X-ray band. The locations of these two sources (2HWC J1104+381 for Mrk 421 and 2HWC J1653+397 for Mrk 501) are the only ones in this catalog that have confirmed extragalactic associations.

At a distance of $z \approx 0.031$ (de Vaucouleurs et al. 1991; Mao 2011), Mrk 421 is a BL Lac type blazar that was the first extragalactic object discovered at very high energies (Punch et al. 1992) and has been extensively studied in both the spectral and time domains.

Mrk 501 is also a BL Lac type blazar, at a distance of $z = 0.033$ (de Vaucouleurs et al. 1991; Mao 2011). This

object was the second blazar to be detected at very high energies (Quinn et al. 1996) and is on average the second brightest extragalactic object emitting in the TeV band.

The fluxes of both objects are known to exhibit strong variability on time scales down to hours or even minutes; see for example Gaidos et al. (1996) for Mrk 421 or Albert et al. (2007) for Mrk 501. A first look at week-long VHE flares and the time dependence of their emission observed with the partial HAWC detector is reported in Lauer et al. (2016). Both higher and lower yearly average fluxes for Mrk 421 than the one listed in Table 3 have been reported in the past (Acciari et al. 2014). A detailed characterization of the VHE variability of Mrk 421 and Mrk 501 and a discussion of their spectral features beyond a power law fit will be the topic of a forthcoming HAWC publication, based on the same data discussed here but resolved into daily time intervals.

5.7. 2HWC J1309-054

This source is found in the point search with a TS value of 25.3. No obvious associations are found in the catalogs. The coordinates correspond to a location out of the Galactic Plane ($b = 57.1^\circ$).

5.8. 2HWC J1809-190

2HWC J1809-190 may be associated with HESS J1809-193 (centered $\sim 0.3^\circ$ away) (Aharonian et al. 2007). H.E.S.S. observed it as an extended source modeled with an ellipse of major and minor axis 0.53° and 0.25° respectively. Suzaku observations confirmed hard extended X-ray emission previously detected by ASCA and suggested a possible PWN origin (Anada et al. 2010). However, subsequent radio observations with the Expanded Very Large Array at 1.4 GHz suggested that the gamma-ray emission could instead originate from a system of molecular clouds on the edge of the SNR G11.0-0.0 shock front (Castelletti et al. 2016) and the gamma source is still considered unidentified.

5.9. 2HWC J1812-126

2HWC J1812-126 may be associated with the TeV source HESS J1813-126 (distance of $\sim 0.1^\circ$). HESS J1813-126 was recently discovered by the H.E.S.S. experiment (Deil et al. 2016) and is still unidentified. The intermediate age pulsar PSR J1813-1246, which has been also detected by *Fermi*-LAT, seems coincident with the position of the H.E.S.S. source and has a spindown luminosity $\dot{E} = 6.2 \times 10^{36}$ erg s $^{-1}$ and a characteristic age of 43 kyr.

5.10. 2HWC J1814-173

2HWC J1814-173 is close by and possibly associated with the TeV source HESS J1813-178 (distance

of $\sim 0.5^\circ$), which was detected during the first H.E.S.S. Galactic Plane survey (Aharonian et al. 2005a, 2006b). HESS J1813-178 is a candidate PWN, powered by the highly energetic young pulsar PSR J1813-1749 located close to the center of supernova remnant G12.82-0.02 (Gotthelf & Halpern 2009). PSR J1813-1749 has a spin-down luminosity of $\dot{E} = 6.8 \times 10^{37} \text{ erg s}^{-1}$, a characteristic age of 3.3–7.5 kyr (Gotthelf & Halpern 2009), and an estimated distance of 4.8 kpc (Halpern et al. 2012). Closer to the measured HAWC location is SNR G013.5+00.2 (0.2° away), though it has not been detected in gamma rays by H.E.S.S. or *Fermi*-LAT.

5.11. 2HWC J1819-150*

2HWC J1819-150* is 0.5° away from the nearest source listed in TeVCat, SNR G015.4+00.1 (HESS J1818-154). This source is reported by H.E.S.S. as a point source, which given the distance to the HAWC location makes the association uncertain. Closer to the measured HAWC location is SNR G015.9+00.2 (0.1° away), though it has not been detected in gamma rays by H.E.S.S. or *Fermi*-LAT. There are also 5 ATNF pulsars within 0.5° from 2HWC J1819-150*: PSR J1819-1458 ($\sim 0.1^\circ$, $\dot{E} = 2.9 \times 10^{32} \text{ erg s}^{-1}$, $d = 3.3 \text{ kpc}$, $\tau = 117 \text{ kyr}$), PSR J1819-1510 ($\sim 0.2^\circ$, $\dot{E} = 2.7 \times 10^{31} \text{ erg s}^{-1}$, $d = 4.1 \text{ kpc}$, $\tau = 457 \text{ Myr}$), PSR J1818-1448 ($\sim 0.3^\circ$, $\dot{E} = 1.1 \times 10^{34} \text{ erg s}^{-1}$, $d = 5.0 \text{ kpc}$, $\tau = 725 \text{ kyr}$), PSR J1818-1519 ($\sim 0.4^\circ$, $\dot{E} = 2.0 \times 10^{32} \text{ erg s}^{-1}$, $d = 5.4 \text{ kpc}$, $\tau = 3.6 \text{ Myr}$), and PSR J1817-1511 ($\sim 0.4^\circ$, $\dot{E} = 5.0 \times 10^{33} \text{ erg s}^{-1}$, $d = 7.3 \text{ kpc}$, $\tau = 2.5 \text{ Myr}$).

5.12. 2HWC J1825-134

2HWC J1825-134 was previously detected by HAWC as 1HWC J1825-133. 2HWC J1825-134 is located between two previously reported TeV sources, HESS J1825-137 and HESS J1826-130, at about 0.4° from both. HESS J1826-130 was recently announced by the H.E.S.S. experiment (Deil et al. 2016) and is still unidentified. HESS J1825-137 was detected by H.E.S.S. (Aharonian et al. 2005a) and was identified as a PWN (e.g. Aharonian et al. 2005b). It is connected to the energetic pulsar PSR J1826-1334 (0.2° away from 2HWC J1825-134, $\dot{E} = 2.8 \times 10^{36} \text{ erg s}^{-1}$, $d = 3.6 \text{ kpc}$, $\tau = 21 \text{ kyr}$). It is generally considered the prototype of offset PWNe. HESS J1825-137 shows an energy dependent morphology at VHE gamma rays towards the south of the pulsar PSR J1826-1334 (Aharonian et al. 2006a). The PWN identification was later confirmed by X-ray observations (Pavlov et al. 2008; Uchiyama et al. 2009) showing a clear detection of an extended PWN. The energy dependent morphology studies of HESS J1825-137 continued

in the *Fermi*-LAT era (Grondin et al. 2011; Acero et al. 2013), strengthening the key role of this source in understanding the physics of PWNe. The extension of the TeV spectrum at higher energies by HAWC is in line with this scenario. With more HAWC data, future analysis including multiple source fit will help disentangle the different components contributing to 2HWC J1825-134.

We note that in the present map, the TeV binary LS 5039 is 1.4° away from 2HWC J1825-134 and is included in its TS halo in the maps presented here. Dedicated studies are being developed to separate emission from LS 5039 from 2HWC J1825-134.

5.13. 2HWC J1829-070

This source is found in the point search with a TS value of 25.3. It is located slightly off the Galactic Plane at $b = 8.09^\circ$, and no associations are found in the catalogs within a 0.5° radius.

5.14. 2HWC J1831-098

2HWC J1831-098 may be associated with the TeV source HESS J1831-098 (distance of 0.01°). HESS J1831-098 was detected by the H.E.S.S. experiment in 2011 (Sheidaei et al. 2011), and is a candidate PWN powered by the nearby 67 ms pulsar PSR J1831-0952 ($\dot{E} = 1.1 \times 10^{36} \text{ erg s}^{-1}$, $d = 3.7 \text{ kpc}$, $\tau = 128 \text{ kyr}$). The differential flux at 7 TeV measured by HAWC is two to five times larger than the one reported by H.E.S.S., depending on the source size used in the spectrum fit. The indices measured by HAWC are also softer than the value reported by H.E.S.S., -2.1 ± 0.1 .

5.15. 2HWC J1837-065

2HWC J1837-065 is the principal maximum of an elongated region containing multiple known extended sources which are not resolved in the present analysis. 2HWC J1837-065 may be associated with the close by TeV source HESS J1837-069 (distance of $\sim 0.4^\circ$). HESS J1837-069 can be considered a candidate PWN (Aharonian et al. 2006b; Tibolla et al. 2013). This elongated HAWC region also covers the location of the unidentified H.E.S.S. source HESS J1841-055, which is a very complex TeV gamma-ray source with many potential counterparts, including two SNRs (Kes 73, G26.6-0.1), three high spindown pulsars: PSR J1841-0524 ($\dot{E} = 1 \times 10^{35} \text{ erg s}^{-1}$, $d = 4.1 \text{ kpc}$, $\tau = 30 \text{ kyr}$), PSR J1838-0549 ($\dot{E} = 1 \times 10^{35} \text{ erg s}^{-1}$, $d = 4.0 \text{ kpc}$, $\tau = 112 \text{ kyr}$), and PSR J1837-0604 ($\dot{E} = 2 \times 10^{33} \text{ erg s}^{-1}$, $d = 4.8 \text{ kpc}$, $\tau = 34 \text{ kyr}$), and an X-ray binary (AX J1841.0-0536). ARGO-YBJ also detected emission from this region, ARGO J1839-0627 (Bartoli et al. 2013a). This HAWC region will be studied further in a dedicated analysis.

5.16. *2HWC J1844-032*

2HWC J1844-032 was previously reported by HAWC as 1HWC J1844-031c. It has two positionally compatible TeV gamma-ray sources: HESS J1844-030 ($\sim 0.2^\circ$ distance) and HESS J1843-033 ($\sim 0.3^\circ$ distance). The TeV detected, well studied, PWN Kes 75 (Djannati-Ataï et al. 2008) is slightly offset from the HAWC source (0.6° away). HESS J1844-030 was recently announced by the H.E.S.S. experiment (Deil et al. 2016) and is still unidentified. The following sources are possible associations: G29.4+0.1, AX J1844.6-0305, and PMN J1844-0306; SNR or PWN scenarios are considered reasonable. AX J1844.6-0305 was discovered by Vasisht et al. (2000) and appears in the ASCA GIS data as a bright source and is not yet identified. PMN J1844-0306 is a complex radio/IR region as described by Vasisht et al. (2000).

The other nearby TeV known source, HESS J1843-033 (Hoppe et al. 2008), is a large source with several possible counterparts. A possible X-ray counterpart is AX J1843.8-0352 (G28.60.1), which is an SNR with a peculiar morphology. Chandra (Ueno et al. 2003) discovered a new source within AX J1843.8-0352, CXO J184357-035441, which exhibits a thin thermal spectrum and a jetlike tail. Other possibilities could be AX J1845.0-0258, which has been considered as an anomalous X-ray pulsar (AXP), or SNR G28.8+1.5, whose outer shells may interact with some undiscovered molecular clouds. Further multiwavelength observations are crucial to identify the origin of the VHE emission.

5.17. *2HWC J1847-018*

2HWC J1847-018 was previously detected by HAWC as 1HWC J1849-017c. It may be associated with the unidentified TeV gamma-ray source HESS J1848-018 ($\sim 0.2^\circ$ distance). HESS J1848-018 was discovered by the H.E.S.S. experiment in the extended Galactic Plane Survey. It is located in the direction of, but slightly offset from, the star-forming region W 43 and hence a possible association with it was suggested in Chaves et al. (2008). However the association with the star-forming region has not been further confirmed and this source is now considered to be a candidate PWN following recent observations by *Fermi*-LAT (Acero et al. 2013). Further multiwavelength studies are needed to properly identify the source.

5.18. *2HWC J1849+001*

2HWC J1849+001 may be associated with the extended TeV source HESS J1849-000 ($\sim 0.2^\circ$ distance) (Terrier et al. 2008), which is coincident with the INTEGRAL source IGR J18490-0000. Further X-ray observations by XMM-Newton and RXTE revealed that

IGR J18490-0000 is a Pulsar/PWN system, where a young and very energetic pulsar ($\dot{E} = 9.8 \times 10^{36}$ erg s $^{-1}$, $\tau = 43$ kyr, distance unknown) is powering the system and a compact PWN is detected in the X-ray observations (Gotthelf et al. 2011).

5.19. *2HWC J1852+013**

2HWC J1852+013* is a new TeV detection by HAWC. There is no known gamma-ray sources close to this location; the nearest is the GeV source 3FGL J1852.8+0158, located 0.6° from the central position of 2HWC J1852+013*. Given the source location, there may be a significant contribution of the Galactic diffuse emission to this source.

Multiwavelength catalog searches reveal several pulsars, several X-ray sources and HII regions in the vicinity of 2HWC J1852+013*. Chandra observations exist of a star cluster and infrared dark cloud IRDC G34.4+0.23 and NaSt1 (WR 122), a Wolf-Rayet binary.

The following pulsars are located close by: PSR J1851+0118 ($\sim 0.1^\circ$, $\dot{E} = 7.2 \times 10^{33}$ erg s $^{-1}$, $d = 5.6$ kpc, $\tau = 105$ kyr) and PSR J1850+0124 ($\sim 0.5^\circ$, $\dot{E} = 9.5 \times 10^{33}$ erg s $^{-1}$, $d = 3.4$ kpc, $\tau = 5.2$ Gyr).

5.20. *2HWC J1857+027*

2HWC J1857+027 has been previously reported by HAWC as 1HWC J1857+023. It may be associated with the close by TeV source HESS J1857+026 ($\sim 0.1^\circ$ away) (Aharonian et al. 2008b), which was considered a PWN candidate (e.g. Tibolla et al. 2011). Recent MAGIC observations revealed that the VHE emission above 1 TeV can be spatially separated into two sources: MAGIC J1857.2+0263 and MAGIC J1857.6+0297 (Aleksić et al. 2014). They also confirmed the PWN nature of the first source and a molecular cloud association was suggested for the second source. These two MAGIC sources are too close to be distinguishable in the HAWC analysis reported here; but they should be resolved in future analysis including simultaneous fit of multiple sources.

5.21. *2HWC J1902+048**

2HWC J1902+048* has been tagged by the search algorithm in a region that does not have a TeV counterpart. However, it appears to be in a confused region, possibly with a large contribution of the Galactic diffuse emission, and will be better disentangled in future analysis with more data. Long Swift observations with a total of 23 ks have been performed in the region of 2HWC J1902+048*, due to gamma-ray burst GRB140610. There is no possible counterpart in the 3FGL catalog of *Fermi*-LAT, however there are 2 sources from the previous catalogs within 0.5° : 1FGL

J1902.3+0503c (0.2° away) and 2FGL J1901.1+0427 (0.5° away). Catalog searches reveal several pulsars, several X-ray sources and HII regions in the vicinity of 2HWC J1902+048*.

The three closest pulsars in the ATNF catalog are: PSR J1901+0459 ($\sim 0.3^\circ$, $d = 12.3$ kpc), PSR J1901+0435 ($\sim 0.3^\circ$, $\dot{E} = 1.0 \times 10^{33}$ erg s $^{-1}$, $d = 10.3$ kpc, $\tau = 1.3$ Myr), and PSR J1901+0510 ($\sim 0.3^\circ$, $\dot{E} = 5.3 \times 10^{33}$ erg s $^{-1}$, $d = 5.9$ kpc, $\tau = 313$ kyr). These pulsars could be powering a PWN which is still undetected due to the lack of multiwavelength observations.

5.22. 2HWC J1907+084*

2HWC J1907+084* is a new TeV detection by HAWC. Given the source location and TS value (33.1), there may be a large contribution of the Galactic diffuse emission to this source. Multiwavelength catalog searches reveal several pulsars, several X-ray sources, HII regions, and a molecular cloud system coincident with or in the vicinity of 2HWC J1907+084*. The nearest *Fermi*-LAT source is 3FGL J1904.9+0818, located 0.6° away from the central position of 2HWC J1907+084*.

The nearest pulsar from the ATNF catalog is PSR J1908+0839 ($\sim 0.3^\circ$ away, $\dot{E} = 1.5 \times 10^{34}$ erg s $^{-1}$, $d = 8.3$ kpc, $\tau = 1.2$ Myr).

5.23. 2HWC J1908+063 – MGRO J1908+06

2HWC J1908+063 is associated with the PWN MGRO J1908+06, first discovered by the Milagro experiment (Abdo et al. 2007) and latter observed by H.E.S.S. (Aharonian et al. 2009), ARGO-YBJ (Bartoli et al. 2012), VERITAS (Aliu et al. 2014a), and previously by HAWC and reported as 1HWC J1907+062c. This source was considered unidentified until the advent of *Fermi*-LAT which shed light on the nature of MGRO J1908+06 and strengthened the PWN scenario to explain its VHE gamma-ray emission (Abdo et al. 2010; Acero et al. 2013). The spectrum measured in this work (see Table 3) under the extended hypothesis is consistent with the spectra obtained by H.E.S.S., VERITAS, and MILAGRO, and lower than the ARGO-YBJ results.

5.24. 2HWC J1912+099

2HWC J1912+099 may be associated with the TeV source HESS J1912+101 ($\sim 0.2^\circ$ distance), which was initially proposed to be a PWN connected to the high spindown luminosity pulsar PSR J1913+1011 ($\dot{E} = 2.9 \times 10^{36}$ erg s $^{-1}$, $d = 4.6$ kpc, $\tau = 169$ kyr) (Aharonian et al. 2008a). ARGO-YBJ also detected emission from this region, ARGO J1912+1026 (Bartoli et al. 2013c). The spectral index they report is consistent with the one by H.E.S.S., but the flux above 1 TeV is

much higher than the value reported by H.E.S.S.: in this energy band, the flux of the H.E.S.S. source corresponds to $\sim 9\%$ of the Crab Nebula flux, while the ARGO-YBJ source flux corresponds to $\sim 23\%$ of the Crab flux. This discrepancy occurred for other ARGO-YBJ sources and has been discussed in literature (Bartoli et al. 2013b). The flux measured with HAWC using the extended source model is in agreement with the H.E.S.S. measurement. Due to the lack of multiwavelength confirmation of the PWN scenario, and based on the detection of a shell like morphology seen with increased observation time by H.E.S.S., Pühlhofer et al. (2015) reclassified HESS J1912+101 as an SNR candidate.

5.25. 2HWC J1914+117*

2HWC J1914+117* is a new TeV detection by HAWC. Given the source location and TS value (33), there may be a large contribution of the Galactic diffuse emission to this source. Multiwavelength catalog searches reveal several pulsars, several X-ray sources, and HII regions coincident with or in the vicinity of 2HWC J1914+117*. There have been seven Swift observations, but the overall exposure is too low to identify a possible counterpart. There are no possible counterparts in the *Fermi*-LAT catalogs.

The pulsars from the ATNF pulsar catalog located in the vicinity of 2HWC J1914+117* are: PSR J1915+1144 (0.1° , $d = 7.2$ kpc), PSR J1915+1149 (0.1° , $d = 14$ kpc), PSR J1913+1145 (0.2° , $\dot{E} = 6.9 \times 10^{33}$ erg s $^{-1}$, $d = 14$ kpc, $\tau = 967$ kyr), and PSR B1911+11 (0.4° , $\dot{E} = 1.2 \times 10^{32}$ erg s $^{-1}$, $d = 3.1$ kpc, $\tau = 14.5$ Myr).

5.26. 2HWC J1921+131

2HWC J1921+131 is a new TeV detection by HAWC. Given the source location and TS value (30.1), there may be a large contribution of the Galactic diffuse emission to this source. Multiwavelength catalog searches reveal several pulsars, several X-ray sources, and a molecular cloud system coincident with or in the vicinity of 2HWC J1921+131. Swift observations exist of the source IGRJ19203+1328. There is no possible counterpart in the *Fermi*-LAT catalogs within a radius of 1° . PSR J1919+1314 is the only nearby pulsar from the ATNF pulsar catalog, 0.4° away. It is an old (2.4 My) pulsar at a distance $d = 13$ kpc and not very energetic ($\dot{E} = 8 \times 10^{32}$ erg s $^{-1}$), making the association unlikely.

5.27. 2HWC J1922+140 – W51C

2HWC J1922+140 is associated with the radio-bright SNR W51C, which is located at a distance of ~ 5.5 kpc

(Sato et al. 2010) and is a middle-aged remnant ($\sim 3 \times 10^4$ yr) with an elliptical shape in radio encompassing a size of $0.6^\circ \times 0.8^\circ$ (Koo et al. 1995). W51C was detected by *Fermi*-LAT in the energy range from 200 MeV to 50 GeV. Jogler & Funk (2016) reported a high-energy break in the energy spectrum of 2.7 GeV and a spectral index beyond the break at $-2.52^{+0.07}_{-0.06}$. In Aleksić et al. (2012), the MAGIC collaboration reported the detection of W51C at the 11σ level and a spectral index of $-2.58 \pm 0.07_{stat} \pm 0.22_{sys}$. Above 1 TeV, MAGIC observes W15C as an elongated region of half width about 0.1° on the long axis.

2HWC J1922+140 is detected by HAWC in the point source search, however the residual map exhibits various excess around the position of the source once the point source modeled has been subtracted. This indicated there may be additional emission farther away from W51C than previously reported. Given the source location, there may be a significant contribution of the Galactic diffuse emission to this extended emission. The spectrum fit is thus performed but using a point source model and an extended source model, with radius 0.9° . The spectrum measurement reported in Table 3 under the point source hypothesis appear to be in agreement with the MAGIC and *Fermi*-LAT results, while the one performed with the extended hypothesis is larger by about a factor 3.

5.28. 2HWC J1928+177 and 2HWC J1930+188 region

In this region, two sources are found in the point search: 2HWC J1928+177 and 2HWC J1930+188. Only the second source is previously detected in TeV, even though the location of the first source has been observed by IACTs. This region also exhibits signs of additional emission, which will be investigated in future analysis.

2HWC J1928+177 is a new TeV source discovered in the point source search. It is likely associated with the pulsar PSR J1928+1746 (0.03° away, $\dot{E} = 1.6 \times 10^{36}$ erg s $^{-1}$, $d = 4.3$ kpc, $\tau = 83$ kyr), the first pulsar discovered in the Arecibo L-band Feed Array (ALFA) survey (Cordes et al. 2006). This pulsar and 2HWC J1928+177 are also within the 99% uncertainty region of the unidentified EGRET source 3EG J1928+1746 which shows significant variability (Hartman et al. 1999a). The *Fermi*-LAT association for this EGRET source is 3FGL J1928.9+1739. However, the 3FGL source position and the 2HWC J1928+177 source position are not consistent within statistical uncertainty. Also note that *Fermi*-LAT reported two analysis flags associated with this source, indicating a significant dependency of the reported source on the choice of the background model and other possible issues with detection or characteriza-

tion of the source. VERITAS has also observed the location of PSR J1928+1746 (Acciari et al. 2010). However, VERITAS only observed a 1.2σ excess at the source position, and set a flux upper limit above 1 TeV at the 99% confidence level assuming a power law distribution with power law index of -2.5 at 2.6×10^{-13} cm $^{-2}$ s $^{-1}$. Even though the power law index assumed by VERITAS is similar to the HAWC measured spectral index, the flux measured by HAWC is about three times larger than the VERITAS limit, which seems to indicate that the spatial extent of PSR J1928+1746 is larger than the PSF of VERITAS.

2HWC J1930+188 is associated with the supernova remnant SNR G054.1+00.3, which is a known TeV source discovered by VERITAS (Acciari et al. 2010). The VERITAS observation is consistent with a point-like source within the resolution of the instrument. SNR G054.1+00.3 hosts a young and energetic pulsar, PSR J1930+1852, at its center ($\dot{E} = 1.2 \times 10^{37}$ erg s $^{-1}$, $d = 7$ kpc, $\tau = 2.9$ kyr). Lu et al. (2001) reported the discovery of a nonthermal X-ray jet that is consistent with a radio extension. It confirms the existence of a PWN in the SNR G054.1+00.3. The spectral indices and fluxes at 7 TeV of VERITAS and HAWC are consistent within statistical and systematic uncertainties. The HAWC measurements indicate that the TeV spectrum associated with SNR G054.1+00.3 extends beyond the VERITAS measured energy range (250 GeV – 4 TeV).

As explained in Section 4.3, the flux has also been calculated under an extended source hypothesis. The radius has been chosen to include the region around 2HWC J1928+177 and 2HWC J1930+188. Table 3 shows that the measured flux for this whole region is significantly larger than the sum of the fluxes of 2HWC J1928+177 and 2HWC J1930+188 under the point source hypothesis, thus favoring extended emission or additional unresolved sources.

5.29. 2HWC J1938+238

2HWC J1938+238 is a new TeV source discovered in the point source search, within the Galactic Plane. There are several optical galaxies, radio galaxies, and an ATNF pulsar within 0.5° around the source location. However, none of these sources are known X-ray or gamma-ray sources. The pulsar, PSR J1940+2337, is located 0.4° away from 2HWC J1938+238 and is a middle age pulsar (113 kyr) with a spindown power $\dot{E} = 1.9 \times 10^{34}$ erg s $^{-1}$ and a distance $d = 8.5$ kpc.

5.30. 2HWC J1949+244

2HWC J1949+244 is a new TeV source discovered within the Galactic Plane. The source is discovered in

the 1° extended search, which, given the low latitude of the source, suggests there can be an important contribution of the Galactic diffuse emission to this source. It is located 0.1° away from the unidentified *Fermi*-LAT source 3FGL J1949.3+2433. The extent of 3FGL J1949.3+2433 is less than 0.1° , which is much smaller than the size of the search in which 2HWC J1949+244 was found. The *Fermi*-LAT measured spectral index of this source is -2.8 ± 0.2 , which is slightly softer than the one measured by HAWC.

The millisecond pulsar PSR J1950+2414 is also located near 2HWC J1949+244 (0.3° , $\dot{E} = 9.4 \times 10^{33} \text{ erg s}^{-1}$, $d = 7.3 \text{ kpc}$, $\tau = 3.6 \text{ Gyr}$). However, this source has not been detected in X-ray or GeV (Knispel et al. 2015).

5.31. 2HWC J1953+294 and 2HWC J1955+285 region

In this region, two sources are found nearby in the point source search: 2HWC J1953+294 and 2HWC J1955+285, none of which has previous TeV detection.

After the HAWC discovery of 2HWC J1953+294, VERITAS observed this source for 37 hours and confirmed the existence of the TeV source. The VERITAS observations of this source will be continued during the 2016–2017 season (Holder et al. 2017). 2HWC J1953+294 is located at 0.2° from the pulsar wind nebula DA 495, which is associated with the supernova remnant G65.7+1.2. It is likely that the 3FGL J1951.6+2926 is associated with the central pulsar of this system (Karpova et al. 2015). A joint analysis of this region with *Fermi*-LAT, VERITAS, and HAWC data is ongoing.

The second new source, 2HWC J1955+285, may be associated with the shell-type supernova remnant SNR G065.1+00.6, located 0.5° away. The first gamma-ray source in the region of SNR G065.1+00.6 was reported by the COS-B satellite as 2CG 065+00 (Swanenburg et al. 1981), then confirmed by the EGRET detection 3EG J1958+2909 (Hartman et al. 1999b). 2HWC J1955+285 is near the energetic *Fermi*-LAT pulsar PSR J1954+2836 (0.2° away, $\dot{E} = 1.0 \times 10^{36} \text{ erg s}^{-1}$, $\tau = 69 \text{ kyr}$). *Fermi*-LAT also reported a nonobservation of the SNR in Acero et al. (2016). Milagro reported a 4.3σ excess at this location (Abdo et al. 2009). MAGIC reported a non detection and set a flux limit at 2–3% of the Crab Nebula flux at 1 TeV (Aleksic et al. 2010).

5.32. Cygnus region

Within Galactic longitude 70° and 85° in the Galactic plane, there are five 2HWC sources. One is potentially part of the very extended emission in the Cygnus Cocoon field, and the rest are mostly associated with known TeV gamma-ray sources.

2HWC J2006+341 is observed with a TS value of 36.9 and is unassociated with any known TeV detections. Milagro has reported a 3.3σ excess at this location. The nearest gamma-ray source is 0.7° away, an unidentified *Fermi*-LAT source 3FGL J2004.4+3338. This source was also reported in the 1FHL catalog but not the 2FHL catalog. Within a 1° radius there are no nearby SNRs from the Manitoba catalog. The nearest pulsar from the ATNF pulsar catalog is PSR J2004+3429, 0.4° away. Its characteristics are $d = 11 \text{ kpc}$, $\dot{E} = 5.8 \times 10^{35} \text{ erg s}^{-1}$, and a characteristic age of 18 kyr.

2HWC J2019+367 is associated with MGRO J2019+37, which has a reported extent of 0.7° from a 2D Gaussian fit (Abdo et al. 2012). The extended Milagro source is resolved into two by VERITAS (Aliu et al. 2014c), VER J2016+371 and VER J2019+368, with brighter emission coming from the latter. The nature of VER J2016+371 is unclear and could be associated with either the supernova remnant CTB 87 or a blazar, both have been detected by *Fermi*-LAT. VER J2019+368 is extended and encompasses two pulsars, PSR J2021+3651 (3FGL J2021.1+3651) and PSR J2017+3625 (3FGL J2017.9+3627), and a star forming region Sh 2-104 that could all contribute to the extended TeV emission (Gotthelf et al. 2016). The spectrum of VER J2019+368 is derived from a circular region of 0.5° radius and is very hard with a photon index of -1.75 ± 0.3 up to 30 TeV. Comparing the integrated flux between 1 and 30 TeV, the 2HWC measurement from a point source assumption is still higher than that of the VERITAS extended assumption. The PSF of this HAWC dataset below 1 TeV is more extended than the 0.5° radius used by VERITAS and the source could be more extended than previously thought. The integrated flux from the extended source fit of the HAWC source is more consistent with the Milagro measurement.

2HWC J2020+403 is likely associated with VER J2019+407 (Aliu et al. 2013). TeV emission from this source is unidentified and is potentially associated with the supernova remnant G78.2+2.1 (e.g. Fraija & Araya 2016) or the gamma-ray pulsar PSR J2021+4026 ($\dot{E} = 1.2 \times 10^{35} \text{ erg s}^{-1}$, $d = 2.1 \text{ kpc}$, $\tau = 77 \text{ kyr}$). The supernova remnant G78.2+2.1 (Gamma Cygni) is detected as extended by *Fermi*-LAT and reported in both the 3FGL and the 2FHL catalogs. The flux observed by HAWC is higher than the one reported from VER J2019+407. HAWC may be measuring multiple emission components.

Diffuse emission in this region with a 2D Gaussian width of $(2.0 \pm 0.2)^\circ$ has been reported by the Fermi collaboration (Ackermann et al. 2011). The GeV diffuse emission is named the Cygnus Cocoon,

and likely originates from a superbubble of freshly accelerated cosmic rays that are confined up to 150 TeV. ARGO J2031+4157 is reported as the counterpart of the Cygnus Cocoon (Bartoli et al. 2014). The 2D Gaussian width of this source is measured to be $(1.8 \pm 0.5)^\circ$ after subtraction of nearby known TeV sources. This is in agreement with the extended emission reported by Milagro, which has a 2D Gaussian width of 1.8° and a spectrum compatible with an extrapolation of the Fermi Cocoon spectrum (Abdo et al. 2012).

2HWC J2031+415 is associated with TeV J2031+4130, a PWN first reported as unidentified in TeV by HEGRA (Aharonian et al. 2002). Various IACTs have reported pointlike or up to 0.2° extended emissions from the pulsar position with consistent spectra (Lang et al. 2004; Albert et al. 2008; Aliu et al. 2014b), while Milagro and ARGO have reported extended emission compatible with the Cygnus Cocoon as mentioned above. The HAWC flux is more consistent with the flux measured by Milagro and ARGO than the IACTs, in agreement with possible additional emission components besides the PWN within the region.

2HWC J2024+417* is detected with $TS = 28.4$ and could be part of the extended morphology of 2HWC J2031+415. It is 0.35° from 3FGL J2023.5+4126, which is associated with the Cygnus Cocoon field. In addition to the diffuse emission, the 3FGL catalog also lists multiple sources associated with the Cygnus Cocoon field.

6. SOURCE POPULATION

A total of 39 sources are identified in the catalog. Two are associated as blazars, two as SNRs, seven as PWNs, and 14 other have possible associations with PWN, SNR, and molecular clouds. The remaining 14 are unassociated.

The majority of the sources in the catalog lie near the Galactic Plane. Figure 11 illustrates the distributions of the sources in Galactic latitude b and longitude l , as well as the sensitivity, for sources within 10° from the Galactic Plane. It can be seen that our sensitivity is highly uniform in a wide band around the Galactic Plane ($-10^\circ < b < 10^\circ$), which is in contrast to IACT surveys (see e.g. Aharonian et al. 2006b). The close to uniform sensitivity in b of this catalog ensures completeness even for (likely nearby) Galactic sources at moderate to large galactic latitudes. Indeed two new sources are found at rather large galactic latitudes: 2HWC J0700+143 at $b = 8.44^\circ$ and 2HWC J1829+070 at $b = 8.09^\circ$). However, the distribution of the newly observed sources peaks within $|b| < 1^\circ$. In Figure 11, the total and new 2HWC source distributions are compared to the known distributions of supernova remnants from

Green (2014) and pulsars with a spindown luminosity $\dot{E} > 10^{34} \text{ erg s}^{-1}$ from Manchester et al. (2005). When taking into account the sensitivity of this catalog in l , the distribution of the new sources is broadly consistent with that of known SNRs and PSRs.

As noted earlier, in the Inner Galactic Plane, the Galactic diffuse emission may have a significant impact the flux measurement of some sources near the TS threshold. The current knowledge of this emission in the TeV regime is limited, and HAWC is uniquely suited to measure this Galactic diffuse emission in the future.

Out of the Galactic Plane, 2HWC J1104+381 (Mrk421) and 2HWC J1653+397 (Mrk 501) are the only sources with known extragalactic association. We also identify four sources, which have no association, but are also very close to the TS threshold indicating that they may be statistical fluctuations. Random fluctuations are expected to appear mostly out of the Galactic Plane since the latter only represents a small fraction of the sky. However, the expected number of false positive in the catalog search is 0.5, so we regard these sources as interesting and certainly worthy of further scrutiny. Overall, the extragalactic sources represent a smaller fraction of the total number of sources than typically observed by other gamma-ray instruments (e.g. $>75\%$ of extragalactic sources in *Fermi*-LAT 2FHL, and about 50% for IACTs in TeVCat). This is due to the sensitivity of HAWC peaking at higher energy than satellites and IACTs, energy where VHE gamma rays are attenuated by interaction with the extragalactic background light (EBL).

7. CONCLUSIONS

The 2HWC catalog is the result of the first search performed with 507 days of data from the fully deployed HAWC Observatory. It is the most sensitive unbiased TeV survey of large regions of the northern sky performed to date. The peak sensitivity of this survey lies around 10 TeV, depending on the source spectrum. This allowed the detection of a total of 39 sources, 16 of which are more than a degree away from sources reported in TeVCat. The source characteristics (location, spectrum, and for some a tentative indication of the extent) were presented, and possible associations were discussed. Twenty-eight sources have no firm associations. Some are in complex regions with nearby sources and refined analysis as well as more statistics will help the source identification. Four sources are found in the extended search only.

HAWC is continuously taking data and the analysis and detector modeling are being refined. Future analyses will include more data, explore the modeling of mul-

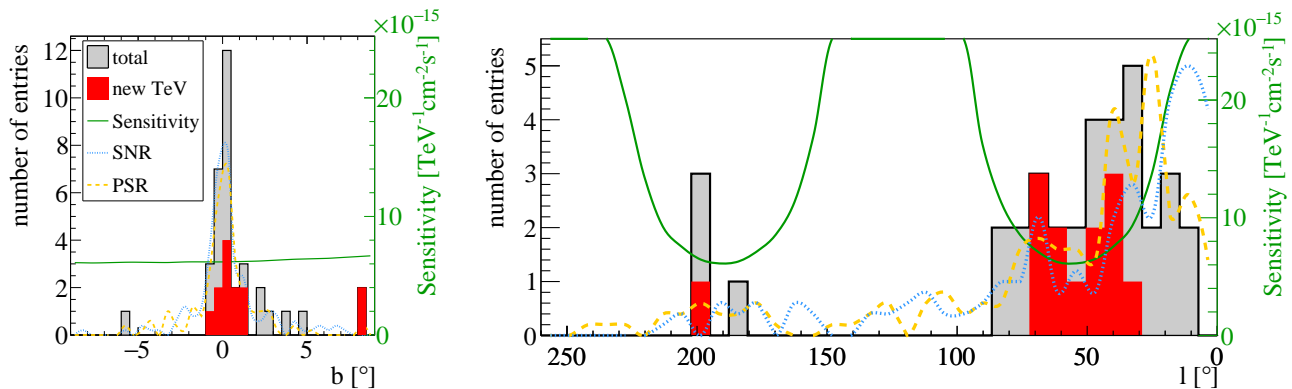


Figure 11. *Left:* Galactic latitude distribution of 2HWC catalog sources in bins of $\Delta b = 0.5^\circ$. *Right:* Galactic longitude distribution in bins of $\Delta l = 7.2^\circ$. The subset of sources without a TeVCat association are shown in red. The right-hand axis on the plot indicate the differential point-source flux sensitivity of the survey at 7 TeV. In the case of the b -distribution, the sensitivity at $l = 60^\circ$ is indicated by the green line and for the l -distribution the sensitivity is shown for $b = 0^\circ$. Both distributions are compared to distributions of known pulsars (Manchester et al. 2005) and supernova remnants (Green 2014) in the field of view of HAWC. Both pulsars and supernova remnants distributions are binned in the same way as the 2HWC sources and re-scaled for ease of comparison. In addition, only pulsars with a spindown luminosity of $\dot{E} > 10^{34} \text{ erg s}^{-1}$ are indicated.

tiple sources and of detailed morphologies making use of multi-instrument and multiwavelength information.

We acknowledge the support from: the US National Science Foundation (NSF); the US Department of Energy Office of High-Energy Physics; the Laboratory Directed Research and Development (LDRD) program of Los Alamos National Laboratory; Consejo Nacional de Ciencia y Tecnología (CONACyT), México (grants 271051, 232656, 260378, 179588, 239762, 254964, 271737, 258865, 243290, 132197), Laboratorio Nacional HAWC de rayos gamma; L’OREAL Fellowship for

Women in Science 2014; Red HAWC, México; DGAPA-UNAM (grants RG100414, IN111315, IN111716-3, IA102715, 109916, IA102917); VIEP-BUAP; PIFI 2012, 2013, PROFOCIE 2014, 2015; the University of Wisconsin Alumni Research Foundation; the Institute of Geophysics, Planetary Physics, and Signatures at Los Alamos National Laboratory; Polish Science Centre grant DEC-2014/13/B/ST9/945; Coordinación de la Investigación Científica de la Universidad Michoacana. Thanks to Luciano Díaz and Eduardo Murrieta for technical support.

REFERENCES

- Abdo, A. A., Allen, B., Berley, D., et al. 2007, *Astroparticle Physics Letters*, 664, L91
- Abdo, A. A., Allen, B., Aune, T., et al. 2008, *ApJ*, 688, 1078
- Abdo, A. A., et al. 2009, *ApJ*, 700, L127, [Erratum: *ApJ*, 703, L185(2009)]
- Abdo, A. A., Ackermann, M., Ajello, M., et al. 2010a, *ApJS*, 188, 405
- . 2010b, *ApJ*, 720, 272
- Abdo, A. A., Ackermann, M., Ajello, M., et al. 2010, *ApJ*, 711, 64
- Abdo, A. A., Abeysekara, U., Allen, B. T., et al. 2012, *ApJ*, 753, 159
- Abdo, A. A., Ajello, M., Allafort, A., et al. 2013, *ApJS*, 208, 17
- Abeysekara, A., Albert, A., Alfaro, R., et al. 2017, submitted to *ApJ*, arXiv:1701.01778
- Abeysekara, A., Alfaro, R., Alvarez, C., et al. 2016, *ApJ*, 817, 3
- Abramowski, A., Aharonian, F., Ait Benkhali, F., et al. 2014, *PhRvD*, 90, 122007
- Acciari, V. A., Aliu, E., Arlen, T., et al. 2010, *ApJL*, 719, L69
- . 2011, *ApJ*, 738, 25
- Acciari, V. A., Arlen, T., Aune, T., et al. 2014, *Astroparticle Physics*, 54, 1
- Acero, F., Ackermann, M., Ajello, M., et al. 2013, *ApJ*, 773, 77
- . 2015, *ApJS*, 218, 23
- . 2016, *ApJS*, 224, 8
- Ackermann, M., Ajello, M., Allafort, A., et al. 2011, *Science*, 334, 1103
- Ackermann, M., Ajello, M., Allafort, A., et al. 2013, *ApJS*, 209, 34

- Ackermann, M., Ajello, M., Atwood, W. B., et al. 2016, *ApJS*, 222, 5
- Aharonian, F., Akhperjanian, A., Beilicke, M., et al. 2002, *A&A*, 393, L37
- Aharonian, F., Akhperjanian, A. G., Aye, K.-M., et al. 2004, *Astroparticle Physics*, 22, 109
- . 2005a, *Science*, 307, 1938
- Aharonian, F., Akhperjanian, A. G., Bazer-Bachi, A. R., et al. 2006a, *A&A*, 460, 365
- . 2006b, *ApJ*, 636, 777
- . 2007, *A&A*, 472, 489
- Aharonian, F., Akhperjanian, A. G., Barres de Almeida, U., et al. 2008a, *A&A*, 484, 435
- . 2008b, *A&A*, 477, 353
- Aharonian, F., Akhperjanian, A. G., Anton, G., et al. 2009, *A&A*, 499, 723
- Aharonian, F. A., Atoyan, A. M., & Voelk, H. J. 1995, *A&A*, 294, L41
- Aharonian, F. A., Akhperjanian, A. G., Barrio, J. A., et al. 2001, *A&A*, 366, 62
- Aharonian, F. A., Akhperjanian, A. G., Bazer-Bachi, A. R., et al. 2005b, *A&A*, 442, L25
- Ahnen, M. L., et al. 2016, *A&A*, 591, A138
- Albert, J., Aliu, E., Anderhub, H., et al. 2006, *ApJL*, 638, L101
- Albert, J., et al. 2007, *Astrophys. J.*, 669, 862
- Albert, J., Aliu, E., Anderhub, H., et al. 2008, *ApJL*, 675, L25
- Aleksic, J., et al. 2010, *Astrophys. J.*, 725, 1629
- Aleksić, J., Alvarez, E. A., Antonelli, L. A., et al. 2012, *A&A*, 541, A13
- Aleksić, J., Ansoldi, S., Antonelli, L. A., et al. 2014, *A&A*, 571, A96
- . 2016, *Astroparticle Physics*, 72, 61
- Aliu, E., Archambault, S., Arlen, T., et al. 2013, *ApJ*, 770, 93
- Aliu, E., Archambault, S., Aune, T., et al. 2014a, *Astroparticle Physics*, 787, 166
- Aliu, E., Aune, T., Behera, B., et al. 2014b, *ApJ*, 783, 16
- . 2014c, *ApJ*, 788, 78
- Anada, T., Bamba, A., Ebisawa, K., & Dotani, T. 2010, *PASJ*, 62, 179
- Anderhub, H., Backes, M., Biland, A., et al. 2011, *Nuclear Instruments and Methods in Physics Research A*, 639, 58
- Ansoldi, S., Antonelli, L. A., Antoranz, P., et al. 2016, *A&A*, 585, A133
- Atkins, R., Benbow, W., Berley, D., et al. 2003, *ApJ*, 595, 803
- Atkins, R., Benbow, W., Berley, D., et al. 2004, *ApJ*, 608, 680
- Atoyan, A. M., & Aharonian, F. A. 1996, *MNRAS*, 278, 525
- Bacci, C., Bao, K., Barone, F., et al. 2002, *Astroparticle Physics*, 17, 151
- Bartoli, B., Bernardini, P., Bi, X. J., et al. 2012, *Astroparticle Physics*, 760, 110
- . 2013a, *ArXiv e-prints*, arXiv:1303.1258
- . 2013b, *ApJ*, 767, 99
- . 2013c, *ApJ*, 779, 27
- . 2014, *ApJ*, 790, 152
- Brisken, W. F., Thorsett, S. E., Golden, A., & Gross, W. M. 2003, *Astrophys. J.*, 593, L89
- Carrigan, S., et al. 2013, *ArXiv e-prints*, arXiv:1307.4690
- Castelletti, G., Giacani, E., & Petriella, A. 2016, *A&A*, 587, A71
- Chaves, R. C. G., Renaud, M., Lemoine-Goumard, M., & Goret, P. 2008, in *American Institute of Physics Conference Series*, Vol. 1085, 372–375
- Cordes, J. M., Freire, P. C. C., Lorimer, D. R., et al. 2006, *ApJ*, 637, 446
- de Vaucouleurs, G., de Vaucouleurs, A., Corwin, Jr., H. G., et al. 1991, *Third Reference Catalogue of Bright Galaxies*
- Deil, C., et al. 2016, *PoS, ICRC2015*, 773
- Djannati-Ataï, A., deJager, O. C., Terrier, R., Gallant, Y. A., & Hoppe, S. 2008, *International Cosmic Ray Conference*, 2, 823
- Frajia, N., & Araya, M. 2016, *ApJ*, 826, 31
- Gaidos, J. A., Akerlof, C. W., Biller, S., et al. 1996, *Nature*, 383, 319
- Górski, K. M., Hivon, E., Banday, A. J., et al. 2005, *ApJ*, 622, 759
- Gotthelf, E. V., & Halpern, J. P. 2009, *ApJL*, 700, L158
- Gotthelf, E. V., Halpern, J. P., Terrier, R., & Mattana, F. 2011, *ApJL*, 729, L16
- Gotthelf, E. V., Mori, K., Aliu, E., et al. 2016, *ApJ*, 826, 25
- Green, D. A. 2014, *Bulletin of the Astronomical Society of India*, 42, 47
- Gronidin, M.-H., Funk, S., Lemoine-Goumard, M., et al. 2011, *ApJ*, 738, 42
- Halpern, J. P., Gotthelf, E. V., & Camilo, F. 2012, *ApJL*, 753, L14
- Hartman, R. C., Bertsch, D. L., Bloom, S. D., et al. 1999a, *ApJS*, 123, 79
- . 1999b, *ApJS*, 123, 79
- HAWC Collaboration. 2017, in preparation
- Holder, J., Atkins, R. W., Badran, H. M., et al. 2006, *Astroparticle Physics*, 25, 391
- Holder, J., et al. 2017, *AIP Conference Proceedings*, 1792, 020013
- Hoppe, S., et al. 2008, *International Cosmic Ray Conference*, 2, 579

- Jogler, T., & Funk, S. 2016, *ApJ*, 816, 100
- Karpova, A., Zyuzin, D., Danilenko, A., & Shibanov, Y. 2015, *MNRAS*, 453, 2241
- Knispel, B., Lyne, A. G., Stappers, B. W., et al. 2015, *ApJ*, 806, 140
- Koo, B.-C., Kim, K.-T., & Seward, F. D. 1995, *ApJ*, 447, 211
- Lang, M. J., Carter-Lewis, D. A., Fegan, D. J., et al. 2004, *A&A*, 423, 415
- Lauer, R. J., et al. 2016, *PoS, ICRC2015*, 716
- Lu, F. J., Aschenbach, B., Song, L. M., & Durouchoux, P. 2001, *Ap&SSSupplement*, 276, 141
- Manchester, R. N., Hobbs, G. B., Teoh, A., & Hobbs, M. 2005, *AJ*, 129, 1993
- Mao, L. S. 2011, *NewA*, 16, 503
- Nolan, P. L., Abdo, A. A., Ackermann, M., et al. 2012, *ApJS*, 199, 31
- Pavlov, G. G., Kargaltsev, O., & Brisken, W. F. 2008, *ApJ*, 675, 683
- Popkow, A., et al. 2015, *ArXiv e-prints*, arXiv:1508.06684
- Pühlhofer, G., Brun, F., Capasso, M., et al. 2015, *ArXiv e-prints*, arXiv:1509.03872
- Punch, M., Akerlof, C. W., Cawley, M. F., et al. 1992, *Nature*, 358, 477
- Quinn, J., Akerlof, C. W., Biller, S., et al. 1996, *Astroparticle Physics Letters*, 456, L83
- Sato, M., Reid, M. J., Brunthaler, A., & Menten, K. M. 2010, *ApJ*, 720, 1055
- Sheidaei, F., et al. 2011, *International Cosmic Ray Conference*, 7, 244
- Strong, A. W., Moskalenko, I. V., & Ptuskin, V. S. 2007, *Annu. Rev. Nucl. Part. Sci.*, 57, 285
- Swanenburg, B. N., Bennett, K., Bignami, G. F., et al. 1981, *ApJL*, 243, L69
- Terrier, R., Mattana, F., Djannati-Atai, A., et al. 2008, in *American Institute of Physics Conference Series*, Vol. 1085, 312–315
- Tibolla, O., Mannheim, K., Kaufmann, S., & Elsässer, D. 2011, *International Cosmic Ray Conference*, 6, 202
- Tibolla, O., Vorster, M., Kaufmann, S., Ferreira, S., & Mannheim, K. 2013, *ArXiv e-prints*, arXiv:1306.6833
- Uchiyama, H., Matsumoto, H., Tsuru, T. G., Koyama, K., & Bamba, A. 2009, *PASJ*, 61, S189
- Ueno, M., Bamba, A., Koyama, K., & Ebisawa, K. 2003, *ApJ*, 588, 338
- Vasisht, G., Gotthelf, E. V., Torii, K., & Gaensler, B. M. 2000, *ApJL*, 542, L49
- Wakely, S. P., & Horan, D. 2008, *International Cosmic Ray Conference*, 3, 1341
- Weekes, T. C., et al. 1989, *ApJ*, 342, 379
- Younk, P. W., Lauer, R. J., Vianello, G., et al. 2016, *PoS, ICRC2015*, 948
- Yüksel, H., Kistler, M. D., & Stanev, T. 2009, *PhRvL*, 103, 051101